Lower Critical Fields, Penetration Depth, and Energy Dissipation of Flux Motion in Bi-Sr-Ca-Cu-O Single Crystals

by

Weibing Xing

B.Sc., Ningxia University, 1982

THESIS SUBMITTED IN PARTIAL FULFILLMENT OF
THE REQUIREMENTS FOR THE DEGREE OF
MASTER OF SCIENCE
in the Department
of
Physics

SIMON FRASER UNIVERSITY

February, 1990

APPROVAL

Name: Weibing Xing

Degree: Master of Science

Title of Thesis: Lower Critical Fields, Penetration Depth, and Energy Dissipation of Flux Motion in Bi-Sr-Ca-Cu-O Single Crystals

Examination Committee:

Chairman: E. D. Crozier

S. Gygax
Senior Supervisor

A. E. Curzon

B. P. Clayman

J. C. Irwin
Examiner
Professor
Department of Physics

G. Kirczenow

Date Approved: February 23, 1990

PARTIAL COPYRIGHT LICENSE

I hereby grant to Simon Fraser University the right to lend my thesis, project or extended essay (the title of which is shown below) to users of the Simon Fraser University Library, and to make partial or single copies only for such users or in response to a request from the library of any other university, or other educational institution, on its own behalf or for one of its users. I further agree that permission for multiple copying of this work for scholarly purposes may be granted by me or the Dean of Graduate Studies. It is understood that copying or publication of this work for financial gain shall not be allowed without my written permission.

Title of Thesis/Project/Extended Essay

Lower Critical Fields, Penetration Depth, and Energy Dissipation of Flux Motion in Bi-Sr-Ca-Cu-O Single Crystals

Author: _____
(signature)

Weibing Xing
(name)

April 11, 1990
(date)

Abstract

Single crystals of $Bi_2Sr_2Ca_1Cu_2O_8$ high critical temperature superconductors were obtained by a flux-growth method. The actual chemical composition was determined by energy dispersive x-ray analysis. The x-ray diffraction patterns on the a-b basal plane could be indexed with the crystal lattice constant $c \approx 30.81 \pm 0.04$ Å.

By using a SQUID magnetometer, low field magnetization measurements have been performed, from which values of lower critical fields at 4.2 K for one of the good quality single crystals were determined: $H_{c1}^{\parallel} \approx 2.2 \pm 0.2$ Oe and $H_{c1}^{\perp} \approx 149 \pm 21$ Oe for a magnetic field applied parallel and perpendicular to the crystalline basal plane respectively. The anisotropy in H_{c1} due to the layered structure is then 68 ± 11, much larger than that of $Y_1Ba_2Cu_3O_{7-\delta}$ single crystals.

The temperature dependent magnetic penetration depth $\lambda_{\parallel}(T)$ for supercurrents flowing in the ab-plane was obtained from a measurement of the AC susceptibility. $\lambda_{\parallel}(T)$ follows the prediction of the clean local limit weak-coupling BCS theory, suggesting an s-wave pairing mechanism. By using a two-parameter least-square fitting process, the zero temperature penetration depth $\lambda_{\parallel}(0)$ was extrapolated to be 2900 Å, which, together with the London formula, implies a carrier density of the order of 3×10^{21} carriers/cm^3.

Within the framework of the anisotropic Ginzburg-Landau theory, the effective mass ratio, $\gamma^2 = M/m \sim 1.2 \times 10^4$, was derived from our measurement. This giant effective mass anisotropy indicates two-dimensional superconducting behavior.

The zero temperature equilibrium supercurrent densities at H_{c1} were estimated by using Maxwell's equations, $J_{cd\parallel} \sim 4 \times 10^6$ A/cm^2 and $J_{cd\perp} \sim 6 \times 10^2$ A/cm^2. The supercurrents thus flow much more easily in the ab-plane than between the planes.

Energy dissipation in flux motion in single crystals was obtained from measurements of the complex AC susceptibility $\chi = \chi' + i\chi''$. The field versus

temperature line defined from the peak positions of the imaginary component χ'' is interpreted to be closely correlated to the irreversibility line in the low field domain.

Acknowledgements

I would like to thank my supervisor Dr. Suso Gygax for his guidance throughout this work.

I would also like to express my appreciations to co-worker Mr. Deming Song for his cooperation in crystal growth and to visiting professor Dieter Meier for many technological assistances and enlightening discussions.

I am very grateful to Dr. Onkar S. Rajora for his assistance in sample analyses with the electron microscope and to Mr. Vern Moen for his help in making drawings for this thesis.

Contents

List of Tables

List of Figures

Chapter 1 Introduction

High critical temperature (high-T_c) superconductivity was discovered by the Nobel Prize laureates, J. G. Bednorz and K. A. Muller, in 1986. Since then this research has been spreading worldwide and developing rapidly in the fields of practical applications as well as basic condensed matter physical sciences. This thesis was undertaken to investigate the low field magnetic properties of single crystals of $Bi_2Sr_2Ca_1Cu_2O_8$, a member of the high-T_c copper oxide families, by using a SQUID magnetometer.

Chapter 1 starts with a brief review on the development of high-T_c superconductivity, and then the descriptions of basic thermodynamic phenomena and the anisotropic Ginzburg-Landau theory. Chapter 2 shows the methods of growing single crystals and sample analysis. Chapter 3 is devoted to the description of the SQUID magnetometer and the procedures for the low field magnetic measurement. Chapter 4 presents the results and discussions. Chapter 5 is a conclusion.

1.1 Review of High-T_c Superconductivity

The new era of high-T_c superconductivity started in 1986 when J. G. Bednorz and K. A. Muller[1] of IBM Zurich Research Laboratory reported the evidence for superconducting behavior near 30 K in a $La_{2-x}Ba_xCuO_4$ compound. Towards the end of the year, the transition temperature was elevated to 40 K by replacing barium with strontium in this formula. Early in 1987, P. Chu and his associates[2] at the University of Houston and the University of Alabama found superconductivity near 92 K in a Y-Ba-Cu-O compound. Its correct chemical composition was then identified as $Y_1Ba_2Cu_3O_{7-\delta}$ (Y-123). A year later, in January 1988, Japanese researchers headed by H. Maeda[3] at Tsukuba Laboratories of the National Research Institute for Materials announced a new family, Bi-Sr-Ca-Cu-O. Later it was found to have two phases:

$Bi_2Sr_2Ca_2Cu_3O_{10}$ (2223) with a T_c of 110 K and $Bi_2Sr_2Ca_1Cu_2O_8$ (2212), the 85 K phase. A month later, in February 1988, a group headed by A. Herman[4] at the University of Arkansas unveiled the superconductivity of Tl-Ba-Ca-Cu-O, a family closely related to that of Bi-Sr-Ca-Cu-O. Like the bismuth compound, it also has two phases: $Tl_2Ba_2Ca_2Cu_3O_{10}$ (2223) the 125 K phase and $Tl_2Ba_2Ca_1Cu_2O_8$ (2212) the 110 K phase. Up to now, the thallium compound (2223) has the highest transition temperature.

The high-T_c copper oxide superconductors mentioned above are all p-type or hole carrier materials. However, a new family of n-type or electron carriers of 24 K $Nd_{2-x}Ce_xCuO_4$ was reported in January 1989 by Y. Tokura et al.[5] This is believed to have significant implications for understanding high-temperature superconductors.[6]

The explorations of high-T_c superconductors have been challenges to both theorists and experimentalists. According to the BCS pairing theory, the attractive electron-electron interaction is formed via phonon or thermal vibrations of the medium. This theory worked successfully for many conventional superconductors but appears to have difficulties to explain high-T_c superconductivity.[7] Therefore, new mechanisms may be required to elucidate those remarkable properties. The high temperature superconductors are promising candidates in both small-scale and large-scale applications.

1.2 Basic Phenomena and Vortex Structure

Superconductors can be classified into two types in terms of the surface energy associated with the interface between a normal and a superconducting region. When the Ginzburg-Landau (G-L) parameter, $\kappa = \lambda/\xi$, is less or greater than $1/\sqrt{2}$, the

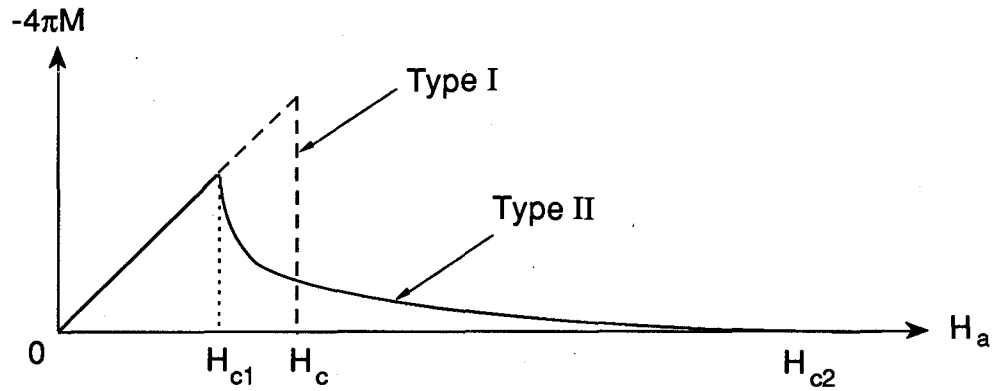

Fig. 1.1 Schematic variation of the magnetization versus applied field in a type I (dashed line) and a type II (solid line) superconductor in the shape of a long cylinder.

superconductor has a positive or negative surface energy corresponding respectively to type I or type II superconductivity. λ is the magnetic penetration depth, the length scale over which the magnetic field is attenuated; and ξ is the coherence length, the length scale over which the order parameter can vary. Fig. 1.1 shows the different magnetic behavior for both types of superconductors, assuming the samples are in the shape of long cylinders to avoid complications of demagnetization effects.

So far the high-T_c copper oxide superconductors have been found to be strongly type II. In a small applied field H_a, a type II superconductor will induce a surface supercurrent so that all the flux is expelled from the specimen except for a limited length scale λ near the surface, and the sample is in the "Meissner state". When H_a reaches the lower critical field, H_{c1}, the flux starts to penetrate into the specimen because that is energetically more favorable, and the sample transfers into the "mixed state" or "vortex state". According to Abrikosov's theory,[8] a type II superconductor in the mixed state has a periodic two-dimensional array of flux lines (filaments) or the flux lattice, each of which contains a flux quantum ϕ_0 (2.07×10^{-7} G·cm^2). The core of each filament has an approximate radius ξ and is surrounded by a vortex of superconducting electrons extending a distance λ. Superconductivity remains until $H_a = H_{c2}$, the upper critical field. The specimen is then undergoing another second order phase transition into the normal state.

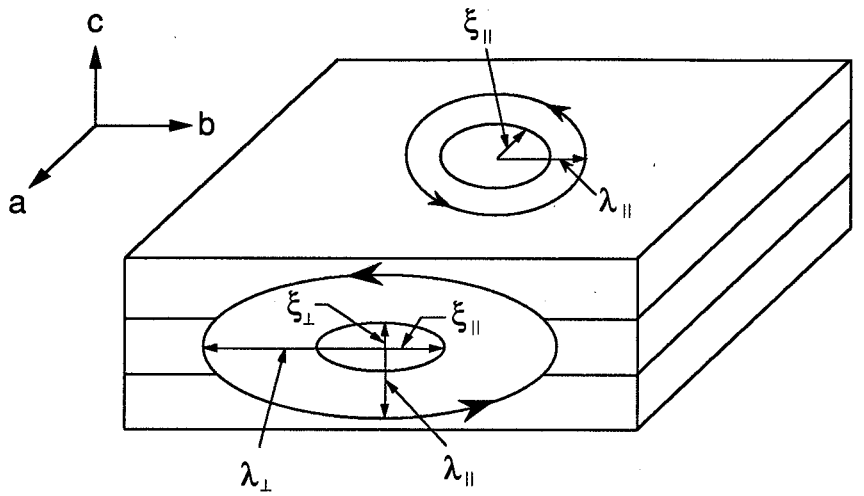

Fig. 1.2. Vortex structure in a layered superconductor illustrating anisotropy of λ and ξ: $\xi_{\perp}$ and $\xi_{\parallel}$ are the coherence length parallel and perpendicular to the ab-plane (Cu-O plane); $\lambda_{\perp}$ and $\lambda_{\parallel}$ are the penetration depth with the supercurrent flowing parallel and perpendicular to the planes.

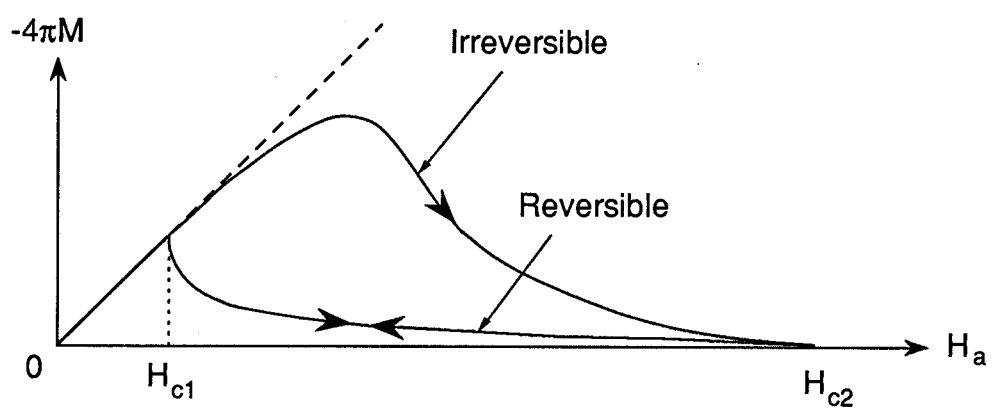

Fig. 1.3. Schematic variations of the magnetization versus field for an ideal (reversible) type II superconductor and a hard (irreversible) superconductor.

The high-T_c superconductors are all found to be layered compounds. Fig. 1.2 shows the vortex structure in a layered superconductor. For a field applied along crystallographic c direction, the supercurrent flows parallel to the ab-plane (Cu-O plane) and controls the penetration depth $\lambda_{\parallel}$. In a field along a or b direction, the penetration depth between the planes (c direction) is controlled by the supercurrent flowing parallel to the ab-plane and therefore equal to $\lambda_{\parallel}$. Whereas the penetration depth within the ab-plane (along b axis in Fig. 1.2), denoted as $\lambda_{\perp}$, is controlled by the supercurrent flowing perpendicular to the planes. Because the supercurrents and the normal currents as well flow much more easily in the Cu-O planes than perpendicular to them, $\lambda_{\perp}$ is larger than $\lambda_{\parallel}$. The coherence length is also anisotropic: $\xi_{\parallel}$, the coherence length parallel to the plane, is larger than $\xi_{\perp}$, the one perpendicular to the plane. Therefore, the shape of the flux lattice, the normal cores, the values of κ, and the critical fields all depend on the field direction.

Type II superconductors can have pinning centers due to material inhomogeneities, such as twin boundaries and point defects. They are often called "hard" superconductors and exhibit hysteresis of the magnetization and flux trapping in the region between H_{c1} and H_{c2}. Fig. 1.3 illustrates schematically the magnetization curve for an ideal (reversible) type II superconductor and a hard (irreversible) superconductor. Owing to the induced bulk supercurrents inside the hard superconductor, the flux penetrates into the hard superconductor more slowly than it does into the ideal type II superconductor when the applied field H_a is larger than H_{c1}.

1.3 Effective Mass Tensor Ginzburg-Landau Theory

The concept of the phenomenological effective mass tensor G-L theory was first proposed by Ginzburg[9] and later justified on the basis of microscopic theory.[10] Specifically, to describe anisotropic superconductors, the effective mass in the

G-L equations is replaced by an effective mass tensor. In the case of uniaxial superconductors, the effective mass tensor has the simple form:

$$m_{ij} = \begin{pmatrix} m & 0 & 0 \\ 0 & m & 0 \\ 0 & 0 & M \end{pmatrix} \tag{1.1}$$

where m is the effective mass of the superconducting electrons in the layer and M that between the layers, neglecting the anisotropy in the layer. Because the "easy" axes for supercurrent flow lie in the plane, it is natural to assume that M is larger than m.

In the large κ limit, the anisotropic G-L equations have been solved.[11] If we define an effective mass ratio, $\gamma^2 = M/m$†, we can then write:[12]

$$\lambda_{\parallel} = \lambda_{\perp}/\gamma \tag{1.2a}$$

$$\xi_{\perp} = \xi_{\parallel}/\gamma \tag{1.2b}$$

and

$$\kappa_{\perp} = \frac{\lambda_{\parallel}}{\xi_{\parallel}} \tag{1.3a}$$

$$\kappa_{\parallel} = \left(\frac{\lambda_{\perp}\,\lambda_{\parallel}}{\xi_{\parallel}\,\xi_{\perp}}\right)^{1/2} \tag{1.3b}$$

$$\kappa_{\perp} = \kappa_{\parallel}/\gamma \tag{1.3c}$$

where $\kappa_{\parallel}$ and $\kappa_{\perp}$ are the G-L parameters with the applied field parallel and perpendicular to the layers, respectively.

The upper critical fields can also be written in the following anisotropic form:

---

† In some of the literature, the effective mass ratio is expressed as $\varepsilon^2 = m/M$.

$$H_{c2}^{\perp} = \frac{\phi_0}{2\pi\xi_{\parallel}^2} \tag{1.4a}$$

$$H_{c2}^{\parallel} = \frac{\phi_0}{2\pi\xi_{\perp}\xi_{\parallel}} \tag{1.4b}$$

When the applied field is close to H_{c1}, the G-L approach leads to non-linear equations which have to be solved for H_{c1}. Klemm and Clem[13] showed that the G-L free energy of the anisotropic mass in the presence of a magnetic field may be transformed into the isotropic G-L form, so the expression of H_{c1} for the layered superconductors can have a similar form for isotropic superconductors, except that the G-L parameter κ is now anisotropic. Their calculations give, in the large κ limit,

$$H_{c1}^{\perp} = \frac{\phi_0}{4\pi\lambda_{\parallel}^2}(\ln\kappa_{\perp} + 0.5) \tag{1.5a}$$

$$H_{c1}^{\parallel} = \frac{\phi_0}{4\pi\lambda_{\perp}\lambda_{\parallel}}(\ln\kappa_{\parallel} + 0.5) \tag{1.5b}$$

where $H_{c1}^{\parallel}$ and $H_{c1}^{\perp}$ are the lower critical fields parallel and perpendicular to the ab-plane, respectively. Kogan[14] used the London equations and derived similar results.

1.4 Motivations

The lower critical fields are important superconducting quantities in the sense of fundamental research and practical applications. For highly layered $Bi_2Sr_2Ca_1Cu_2O_8$ single crystals, sensitive low field magnetization measurements are useful to determine the anisotropic lower critical fields.

The magnetic penetration depth λ is one of the basic microscopic lengths. Because it is related to the superconducting energy gap, the measurement of the variation of the penetration depth with temperature will provide insight into the pairing mechanism. The absolute value of the penetration depth at zero temperature will give estimates of other fundamental parameters, such as the carrier density and the effective mass of the carriers by using London's equations. The temperature dependence of the low field DC or AC susceptibility reflects the flux penetration and hence directly measures the temperature dependence of the magnetic penetration depth.

Since the energy losses can be detected by the imaginary part of AC susceptibility, measurements of the complex AC susceptibility in various applied DC fields are useful for a qualitative description of flux motion in the crystals.

In the absence of a microscopic theory for the new high-T_c superconductors, we intend to make use of Maxwell's equations as well as the formulas derived from the phenomenological Ginzburg-Landau theory in order to estimate, with our measurement, some superconducting parameters of fundamental interests, for example the G-L parameter, the effective mass ratio, the equilibrium supercurrent density, and so on for the Bi-2212 superconductors.

Chapter 2 Sample Preparation and Analysis

In this chapter, we will present the method of growing our Bi-2212 single crystals and the analysis of their chemical compositions by energy dispersive x-ray spectroscopy and x-ray diffraction patterns.

2.1 Sample Preparation

2.1.1 Single Crystal Growth

The Bi-compound single crystals were obtained by a flux-growth method. A typical procedure, with which Sample Bi-A and Bi-C were grown, is as follows: with the nominal molar ratio Bi:Sr:Ca:Cu = 1:1:3:3 the oxides and carbonates, Bi_2O_3, $SrCO_3$, $CaCO_3$, and CuO, were thoroughly mixed and ground with a mortar and a pestle, where excess CuO and $CaCO_3$ were used as the flux; the powders were then pressed into pellets which in turn were placed in a container (made of gold foil) that lay on the flat surface of an alumina sample holder; using a programmable furnace, the mixture was heated in air to 970 °C at a rate of 200 °C/hr, held at 970 °C for about 1.5 hr, and cooled first to 790 °C at 6 °C/hr and then to the ambient temperature at 18 °C/hr. At the temperature 970 °C, the pellets were completely melted and some of the liquids overflowed the shallow container. After cooling, many pieces of single crystals were found among the solidified flux between the gold foil surface and the alumina. This method is similar to the one used for the growth of $YBa_2Cu_3O_{7-\delta}$ single crystals.[15,16] In a run for another batch of crystals, out of which Bi-H and Bi-I grew, the procedure was slightly different: the powders, with a nominal molar ratio Bi:Sr:Ca:Cu = 2:2:1:2, were contained in an alumina crucible and calcined at 780 °C in air for 20 hr; the pelletized mixture was sintered in air at 980 °C for 2 hr, cooled at 2 °C/hr to 800 °C, and then oven-cooled to room temperature. Crystals were picked up from the fragments of the solid melt which was broken up mechanically.

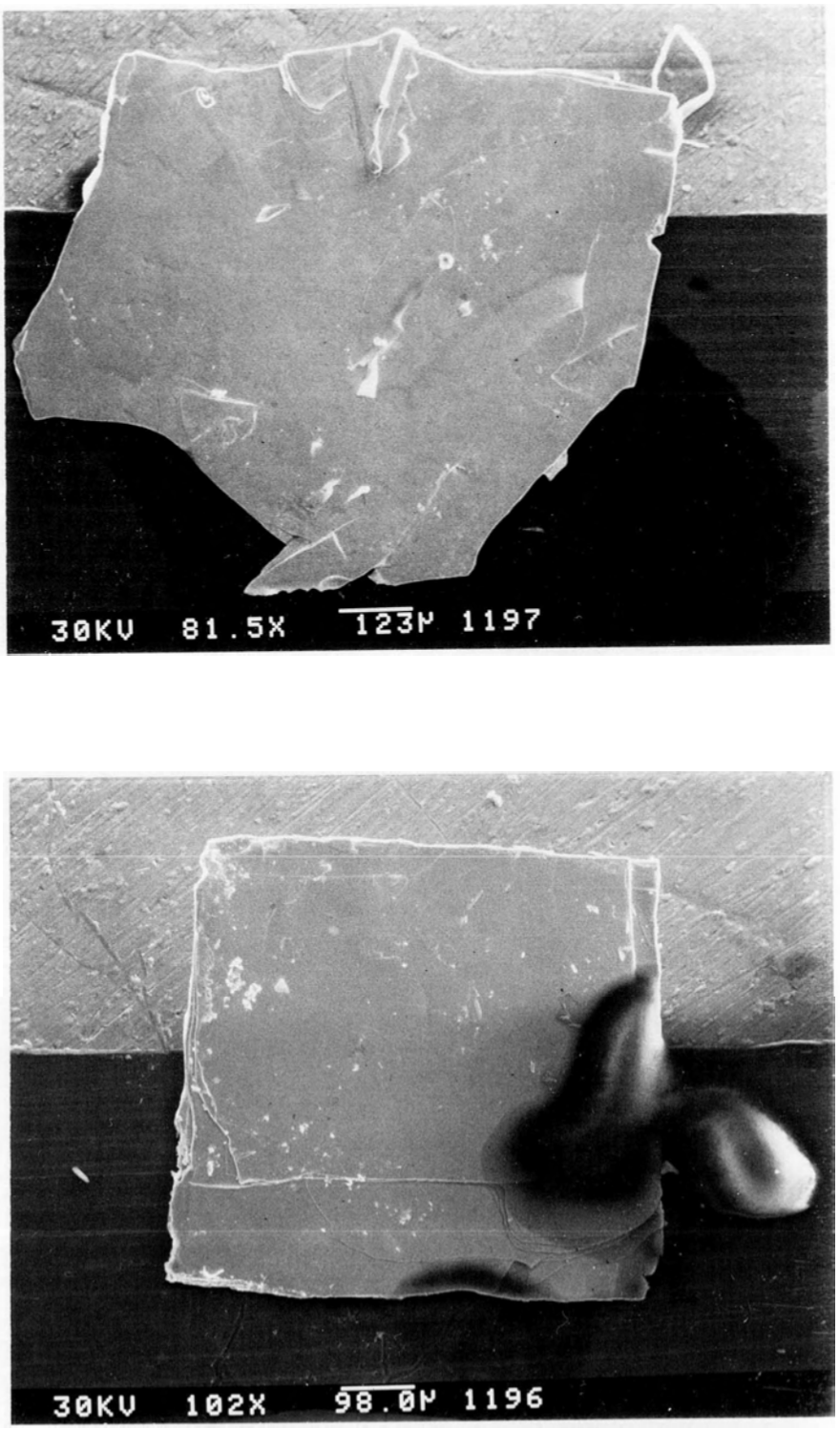

Fig. 2.1. SEM pictures of Samples Bi-H (upper) and Bi-I (lower)

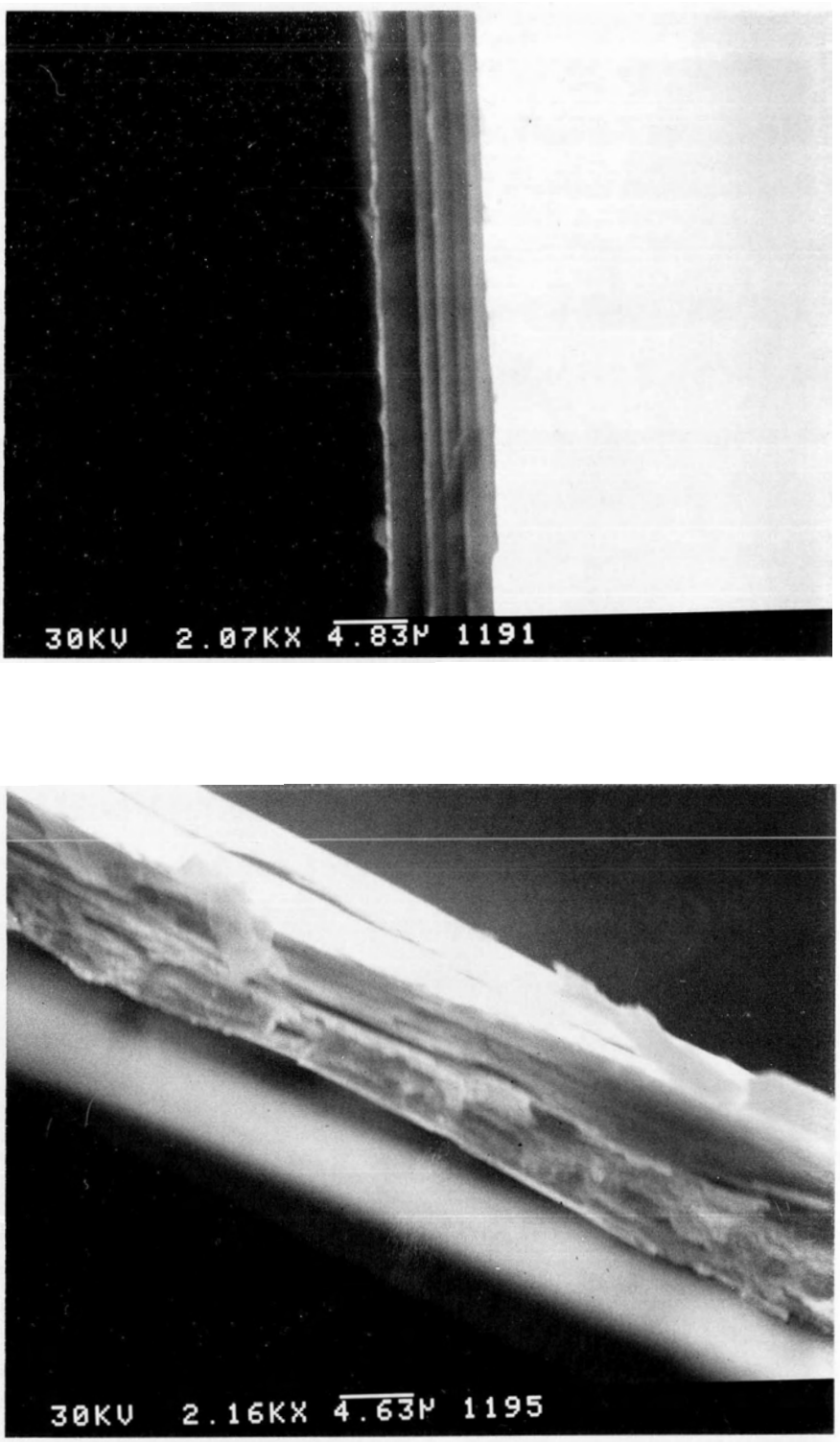

Fig. 2.2. Edge-on SEM pictures of Samples Bi-H (upper) and Bi-I (lower)

2.1.2 Characteristics

The Bi-Sr-Ca-Cu-O single crystals are flaky and brittle. The full size and edge-on pictures of two selected crystals, named as Bi-H and Bi-I, were taken by a Scanning Electron Microscope (SEM, ISI-DS-130), shown in Figs. 2.1 and 2.2. Both crystals have the in-plane dimensions of about 1×1 mm^2 and the thickness of less than 10 μm. Sample Bi-I was cut from a large crystal with a razer blade. The heavy dot seen in the picture on Bi-I is the grease with which the sample was held. Unlike $YBa_2Cu_3O_{7-\delta}$ single crystals that have a rectangular shape and sharp edges,[15,16] the Bi-compound crystals appear to have irregular shapes. The crystals grew favorably in the ab-plane (Cu-O plane) and the crystallographic c direction is the thinnest dimension. The crystals can be easily cleaved with, for example, needles. This makes the material mica-like. It is believed that the weak bond between the bismuth and oxygen is responsible for the cleavage nature.[17] The crystallinity was verified by the x-ray diffraction patterns (see Fig. 2.4).

The transition temperatures of the selected crystals, 85 K for Bi-H and 87 K for Bi-I, were obtained from AC susceptibility measurements. Table 1 shows the real cation ratio given by the energy dispersive x-ray analysis (EG&G, ORTEC). Since the absorption for Ca is only about 0.5 which is below the minimum absorption (~ 0.7) with which the computer program (ZAP Microanalysis) can work optimally, the chemical content of Ca is therefore likely to be underestimated. The same reason may also explain the low atomic percentage of Sr in those formulas. We conclude that within the experimental error, our Bi-based single crystals belong to the 2212 or lower T_c phase.

2.2 Crystal Structure

Electron, neutron, and x-ray diffraction patterns[18-22] have all revealed the complex crystal structure of the Bi-2212 compound. As illustrated in Fig. 2.3, the sheared basic

Table 1. Energy dispersive x-ray analysis for the Bi-Sr-Ca-Cu-O single crystals

Sample	Element	Atomic Percentage	Composition
Bi-H	Bi	30	$Bi_2Sr_{1.75}Ca_{0.82}Cu_2O_{8-\delta}$
	Sr	27	
	Ca	12	
	Cu	30	
Bi-I	Bi	30	$Bi_2Sr_{1.71}Ca_{0.85}Cu_{1.99}O_{8-\delta}$
	Sr	26	
	Ca	13	
	Cu	31	

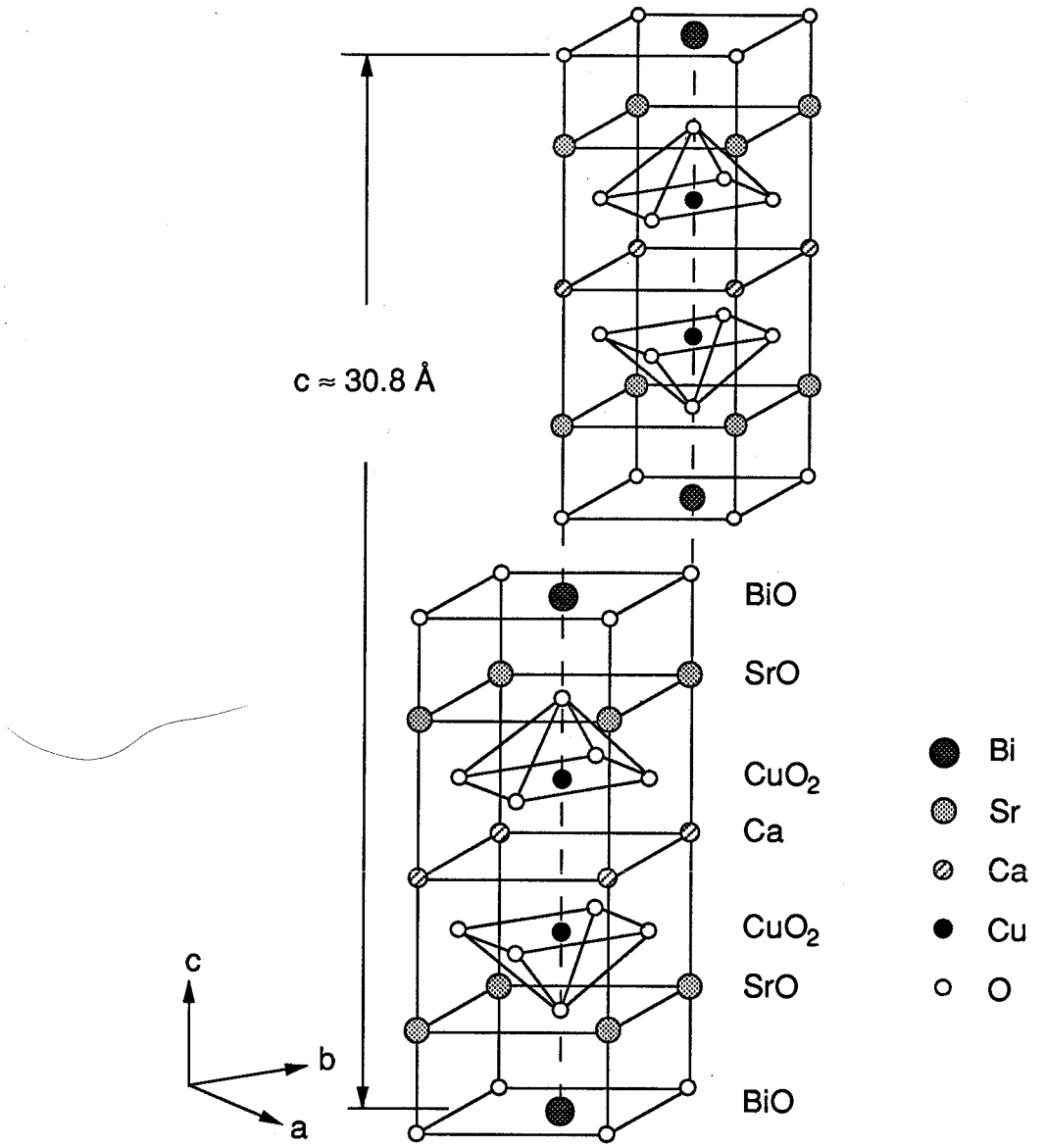

Fig. 2.3 The unit cell of $Bi_2Sr_2Ca_1Cu_2O_8$

building blocks form a tetragonal unit cell with lattice constants: $a \approx b \approx 5.4$ Å and $c \approx 30.8$ Å. Complications arise when the ideal lattice is modulated by, for example, size mismatches, point defects, and so forth,[17] most strongly in the b direction. This modulation results in a periodic superlattice along the b-axis, and the crystal lattice constant b is approximately 5 times that of the ideal unit cell. This superlattice structure has also been observed from the electron diffraction patterns taken on some of our Bi-2212 whiskers.[23]

Fig. 2.4 shows the x-ray diffraction patterns from (0 0 l) planes on one of the Bi-2212 crystals. The diffraction peaks can be indexed with a lattice constant $c \approx 30.81 \pm 0.04$ Å by the standard Hesse-Lipson procedure.[24]

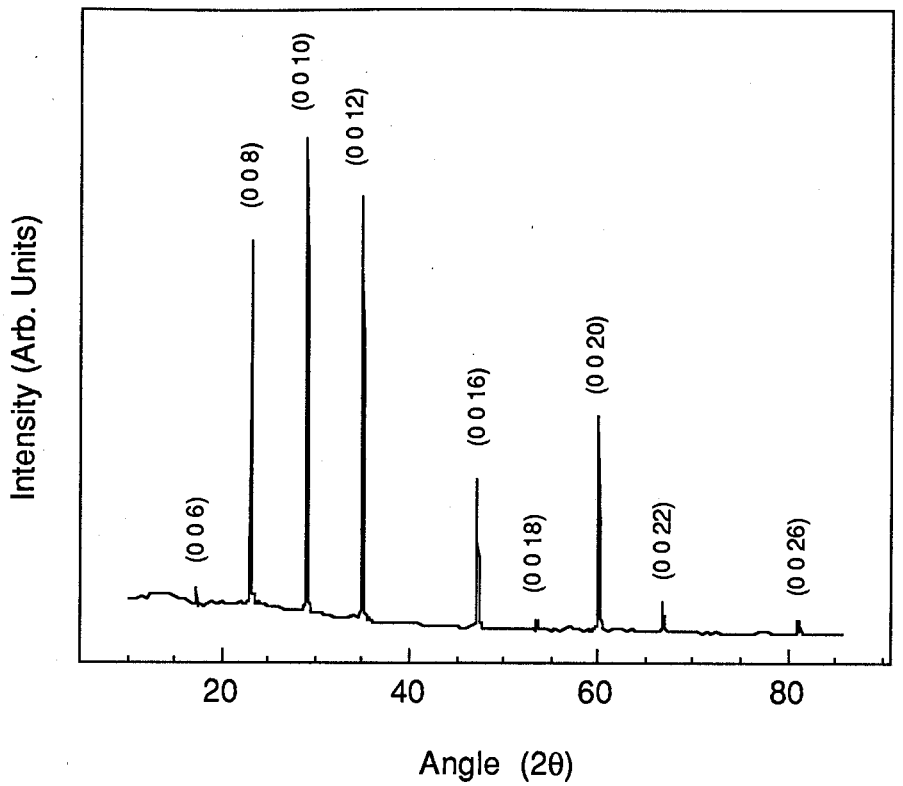

Fig. 2.4. X-ray diffraction patterns of a $Bi_2Sr_2Ca_1Cu_2O_8$ single crystal. Due to the very small thickness of the sample, only the (0 0 ℓ) peaks are visible.

Chapter 3 Experimental Apparatus and Procedure

In this chapter we will describe the main part of the measuring system, the experimental methods of determining the demagnetization factors, and the procedures for low field magnetization measurements.

3.1 Measuring System

A schematic overall view of the main part of the measuring system is shown in Fig. 3.1. The essential component is the Superconducting QUantum Interference Device (SQUID) magnetometer featuring extremely high flux sensitivity and low noise.

3.1.1 Sample Stick

The outline of the sample stick is shown in Fig. 3.1. The thin walled stainless steel tube runs from room temperature to liquid helium temperature (4.2 K) to minimize heat conduction into the bath. The sample space can be evacuated to achieve thermal insulation of the sample from liquid helium. In order to cool the sample, helium exchange gas can be introduced into the sample space through a valve. The sample's position can be changed with an adjuster at the top to get the maximum signal. An enlarged drawing of the lower portion of the sample stick can be seen in Fig. 3.2. The temperature of the sample is controlled by a heater (222 Ω), to which a current of up to 24 mA is applied to warm the sample to about 100 K. A calibrated carbon glass resistor (Lake Shore Cryotronics Inc., Serial C7735) is used as a thermometer. The sample holder is made of sapphire which has good thermal conductivity yet is electrically insulating. The sample is attached to the sapphire rod with Apiezon grease. An Oxygen Free High Conductivity (OFHC) copper block accommodates the heater, the sapphire rod, and the thermometer. Good thermal contact between them is accomplished by tightly fitting with the grease. Under normal operation, the temperature ramp is about 2.5 degrees per minute and the temperature

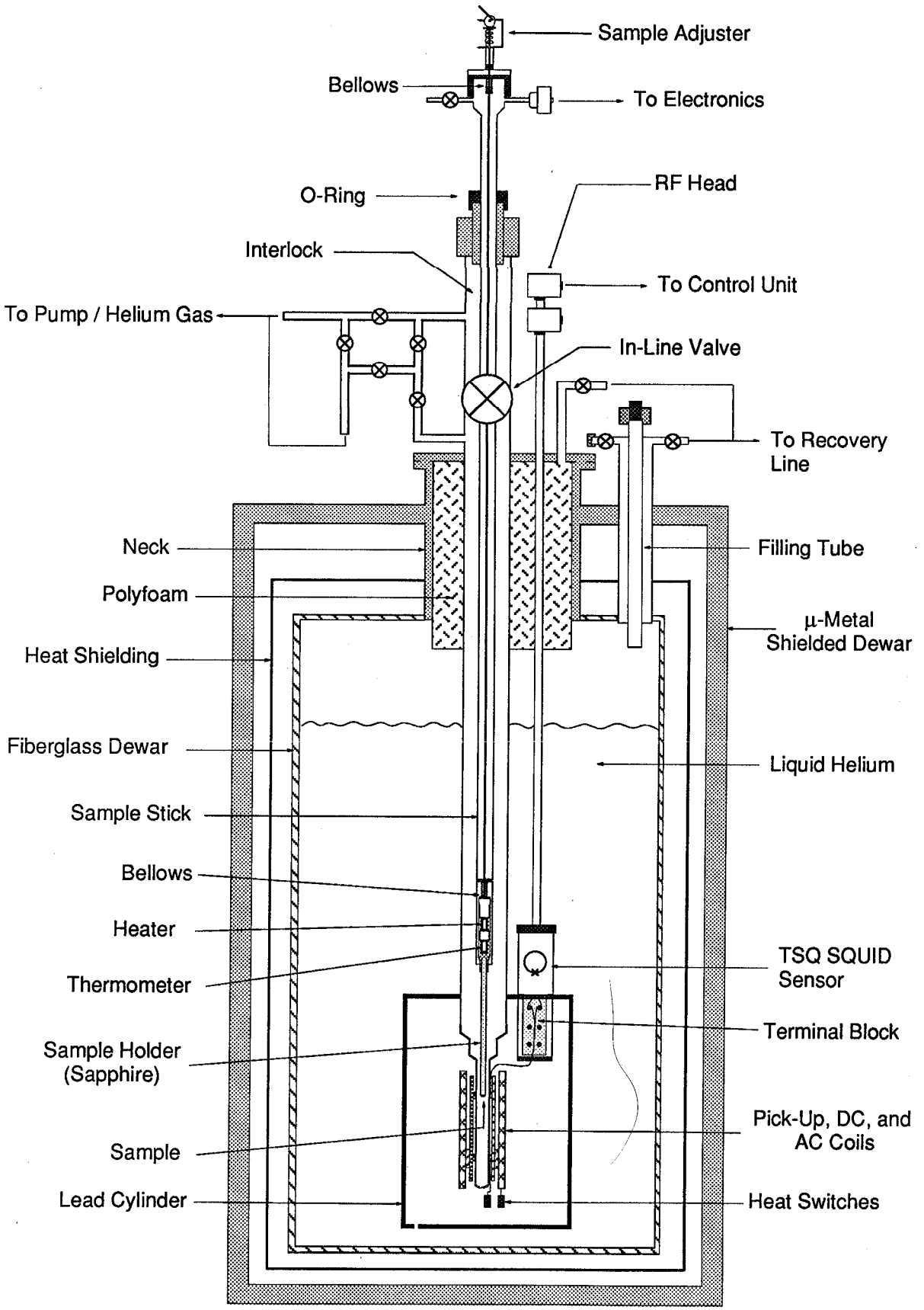

Fig. 3.1. Schematic overall view of the measuring system

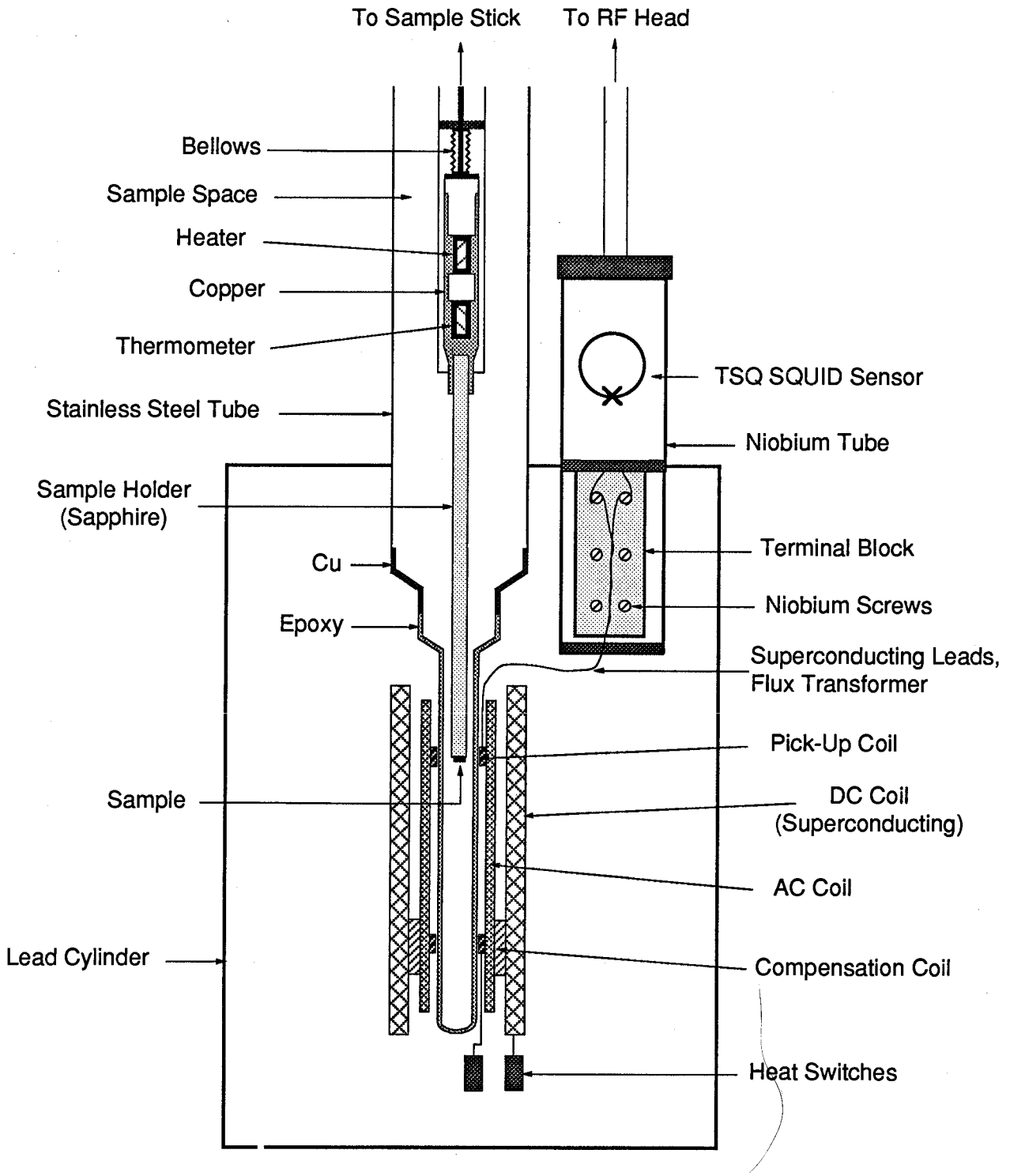

Fig. 3.2 Coil system, SQUID probe, and the lower end of the sample stick (not to scale).

lag between sample and thermometer is less than 0.2 degree in the temperature range of 4.2 K to 100 K. One end of the sapphire rod was machined to such a shape that the sample can be oriented either horizontally or vertically.

3.1.2 Dewar

The commercial dewar (Superconducting Technology Inc.) is drawn schematically in Fig. 3.1. The μ-metal outer shell effectively shields the earth's magnetic field so that the field near the bottom of the dewar is about of the order of mG. This small residual field is regarded as "zero field" in later discussion. A superconducting lead cylinder inside the dewar provides further shielding, for the flux inside the cylinder must remain constant. Liquid helium or nitrogen can be contained in a fiberglass tube. The vacuum space of the dewar is filled with superinsulation. An aluminum thermal shield cooled by the evaporating helium gas absorbs the room temperature radiation. A full dewar of about 13 L liquid helium will normally last for about 3 days.

3.2 Coil System and SQUID Operation

The SHE (Superconducting Helium Electronics) 330 series SQUID system used in this experiment consists of a Toroidal SQUID (TSQ) sensor (a rf-biased weak-link superconducting device), a rf-head, and the control units.

3.2.1 Flux Transformer

The magnetic signal is coupled into the SQUID through a flux transformer, which consists of an astatic pair of pick-up coils wound in series opposition (also called a first order gradiometer), the twisted leads, and a signal coil (see Figs. 3.2 and 3.3). Each of the pick up pair is a seven turn single layered coil made of 0.003" diameter niobium wire. The leads are connected to the terminal board of the SQUID sensor via niobium screws. A complete superconducting loop is thus formed and the flux transformer responds to DC fields as well as to AC signals. The total magnetic flux

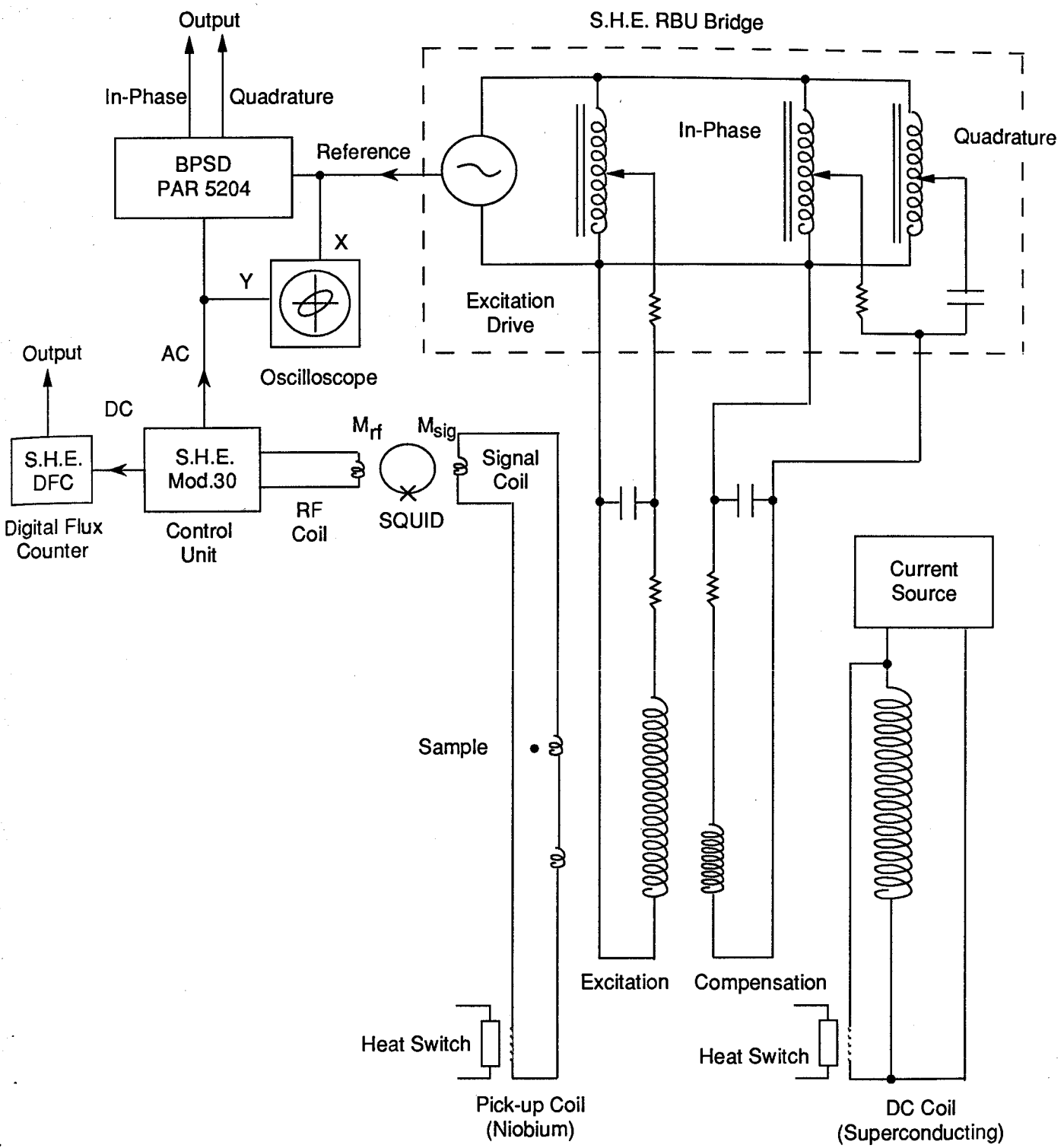

Fig. 3.3 Schematic of the coil system and control unit

threading the flux transformer remains constant at the value it had when the device was cooled through its superconducting transition temperature. If an external flux, ϕ_{ext}, is applied through the transformer coil a current, I_{sq}, will spontaneously begin to circulate along the superconducting wire to keep the total flux constant. This flux is then coupled into the SQUID sensor and in turn into a rf coil through M_{sig} and M_{rf}, the mutual inductances between SQUID and the signal coil, SQUID and rf coil, respectively. The detection of the coupled flux signal is accomplished by the "flux locked" operation to be discussed in 3.2.4.

3.2.2 DC mode

DC current can be injected into the DC coil, wound with superconducting wire, by driving a parallel shunt into the normal state with a heater (see Fig. 3.3). After the heater is turned off, the main coil and the shunt form a closed superconducting loop (all joints are spot welded), therefore the supercurrents circulate in the loop in the "persistent mode". A stable magnetic field produced by the supercurrents can vary from a few mG to 100 G depending on the amount of current injected. A SHE Constant Current Supply is used to provide the DC current. The calibration of the DC field was carried out with a spherical lead sample by measuring the temperature dependence of the critical field $H_c(T)$. The slope of the DC current versus T_c turned out to be ~ 209.4 mA/K, whereas $(dH_c/dT)_{T_c}$ of lead in the literature (e.g. Ref. 25) is ~ 222.13 Oe/K. Consequently, the field/current conversion constant is 1.06 Oe/mA.

3.2.3 AC Mode

A schematic drawing of the AC operation is shown in Fig. 3.3. The SHE Model RBU Low Level AC Impedance Bridge is used as a driving source for the AC excitation and compensation coils. The purpose of using a compensation coil is to modify the out-of-balance signal owing to the fact that in practice the two astatic coils are not exactly identical. The highest AC frequency of the Bridge is 160 Hz, and the amplitude of the

AC field is less than 0.1 Oe. The SQUID sensor in this mode is employed as a low noise null detector. The mutual inductance consisting of a primary and an astatic-pair secondary contains a sample whose magnetic properties are to be studied. There will in general be component voltages induced in the secondary both in phase and out of phase with the drive. Thus, the total mutual inductance can be written in the complex form: M = M' + iM", here M' is proportional to the real component (zero-frequency) of AC susceptibility χ', and M" proportional to the imaginary component χ'' representing energy losses per cycle. The out-of-balance signals of both in-phase and quadrature are detected by a Biphase Lock-In Amplifier (PAR Model 5204) referenced to the operating frequency of the bridge.

3.2.4 Flux Locked Operation

The normal operation[26-28] of the SQUID magnetometer is linearized, i.e. the change in output voltage is made proportional to the magnetic flux coupled into the SQUID. This is achieved by a feedback circuit in the control unit as shown in Figs. 3.4 and 3.5. The 30 MHz rf current excites the tuned tank circuit lightly coupled to the SQUID. In response to the external flux, the output voltage V_{rf} or the transfer function shows the typical "triangle pattern" with a period of exactly one flux quantum ϕ_0. The maxima A and C of the transfer function seen in Fig. 3.5 correspond to the points where the flux in the SQUID is an integer multiple of the flux quantum, whereas the minimum B occurs at the intermediate half integer of the flux quantum. The 50 KHz square wave whose peak-to-peak amplitude is exactly $\phi_0/2$ modulates the external flux.

Assume the system is initially set at point B. If the average external flux differs from the value at B by $\delta\phi$, then the output V_{rf} is:

$$V_{rf} = \frac{2V_0}{\phi_0}\delta\phi \qquad (3.1)$$

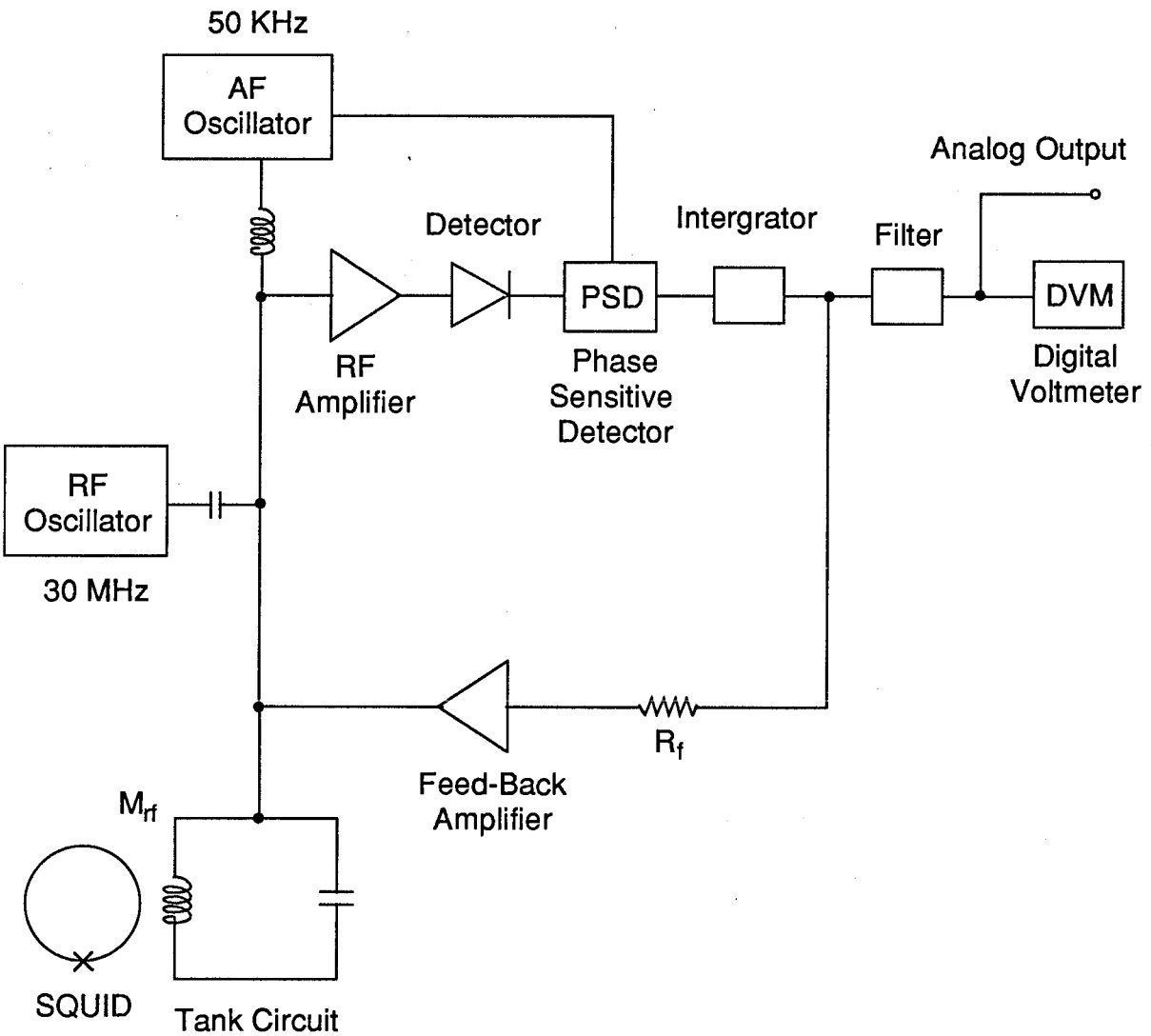

Fig. 3.4 Schematic of the flux-locked operation

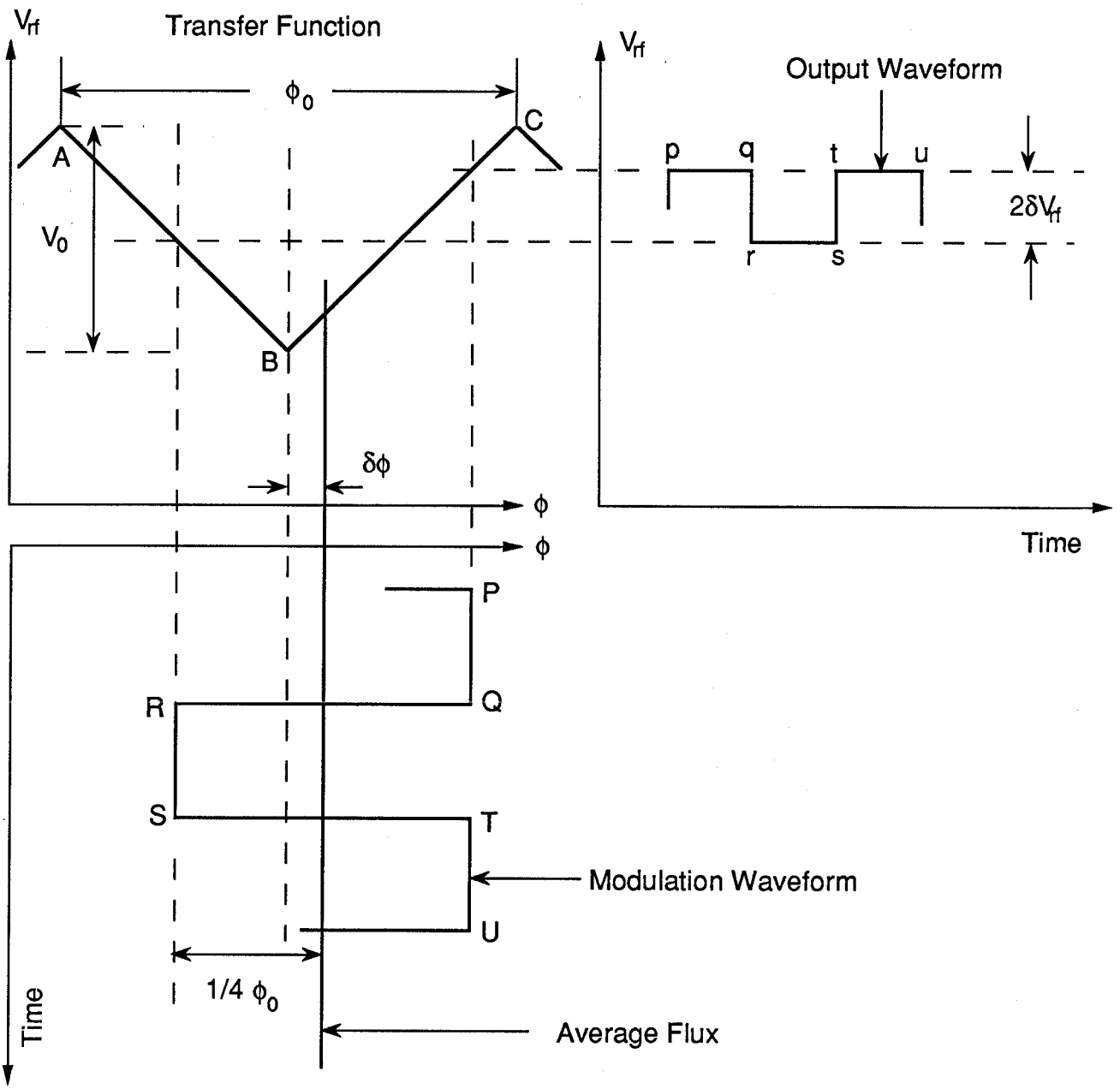

Fig. 3.5 Flux transfer function and flux modulation

where V_0 is the amplitude of the transfer function, and $\delta\phi < 1/4\phi_0$ to ensure the linear operation. After the amplification, a signal proportional to $\delta\phi$ is recovered by a phase sensitive detector at the modulation frequency. The negative feedback current is applied via the feedback resistance R_f to the rf coil and balances the external flux. The average flux in the SQUID is therefore locked at a fixed value corresponding to B. As a result, the output signal proportional to the feedback current is a measure of the external magnetic flux threading the SQUID. It is this linearization that gives rise to the extreme flux sensitivity—with the use of a Digital Flux Counter (SHE, Model DFC), a flux resolution of $10^{-4}\ \phi_0$ and a field sensitivity of better than 10^{-10} G can easily be achieved.

For a complete review on SQUID operation refer to, e.g., References 26-28.

3.3 Experimental Procedure

3.3.1 Flux in Pick Up Coils

The following is mainly a summary of the calculations in Ref. 29.

Because of the special arrangement, the pick up coils, each of which has a radius R and N turns on a common axis with a static applied field H_a, induce a null flux signal when empty. A sample placed in one of the coils can then drive the sensor off null. If a spheroidal sample of radius r and length ℓ are such that $(R-r)/\ell \approx 0$ (that is to say, no return flux through the pick-up loop), then the net flux per gradiometer turn in Gaussian units can be expressed analytically:

$$\phi = (1-D)\phi_m \tag{3.2}$$

where

$$\phi_m = \int (4\pi M)\,ds = \int_0^r (4\pi M)2\pi\rho\,d\rho = 4\pi^2 r^2 \chi H_a (1+4\pi D)^{-1} \tag{3.3}$$

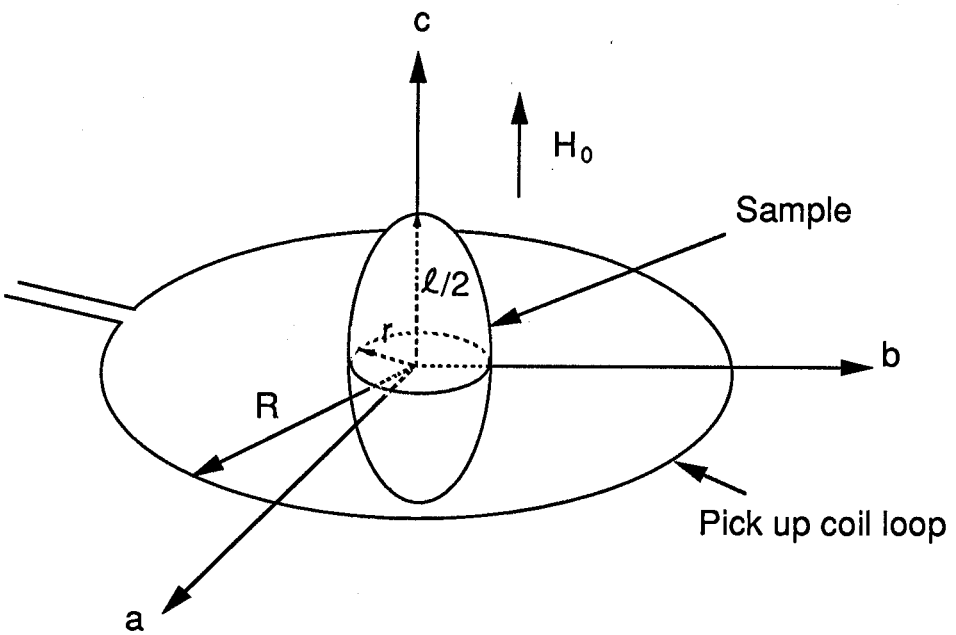

Fig 3.6. One arm of the gradiometer containing a spheroidal sample of central diameter 2r and height ℓ. The pick-up coil has radius R.

is the flux through the sample due to its magnetization, D the demagnetization factor of the sample, and χ the susceptibility M/H_a. In the case of the SQUID flux sensor, complication arises from the requirement that an insulating space be interposed between the sample and the superconducting pick up coils at some temperature higher than the critical temperature of the gradiometer and the SQUID.

To account for the return flux between sample and pick-up loop, noting that the net flux through the loop of radius R is equal and opposite to the flux returning outside the loop (see Fig. 3.6), one can write

$$\phi = -2\pi \int_R^\infty H_m(\rho)d\rho \tag{3.4}$$

where H_m is the magnetization field. Thus the general expression of (3.2) has the form

$$\phi = f\,\phi_m \tag{3.5}$$

where f is called "flux fill factor". From the integration of (3.4) for prolate or oblate spheroids, one obtains f in a closed but somewhat complicated form.[29] When the sample size is small compared with that of the pickup, i.e., $R/r \gg 1$, the magnetic field outside the loop is mainly from the contribution of a dipole. Its radial and tangential components in spherical coordinates are:[30]

$$H_{m\rho} = \frac{2m\cos\theta}{\rho^3} \tag{3.6}$$

$$H_{m\theta} = \frac{m\sin\theta}{\rho^3} \tag{3.7}$$

where m is the dipole moment and θ the azimuthal angle (see Fig. 3.6). Substituting the above H_m into (3.4), one can readily obtain

$$\phi = \frac{2\pi m}{R} = \frac{2\pi VM}{R} = \frac{2\pi V\chi H_a}{R(1+4\pi\chi D)} \tag{3.8}$$

where M = m/V is the magnetization intensity, V the volume of the sample, and the rest defined as previously. The flux fill factor of a dipole then assumes a simple form:

$$f_{dipole}(\varepsilon, R/r) = \frac{2\varepsilon r}{3R} \tag{3.9}$$

where $\varepsilon = m$ for a prolate spheroid and $\varepsilon = 1/m$ for an oblate spheroid; m is defined as the ratio of the long axis to the short axis.

3.3.2 Demagnetization Factor

There is no general solution of the demagnetization factor for samples of arbitrary shape. A general ellipsoid, being specified by the three major axes a, b, and c, can be shown to possess uniform magnetization in a uniform applied field. For such a body, the demagnetization coefficients are analytically calculable and in general, form a demagnetization tensor. Special cases arise where the crystals have rotational symmetries. Assume, for convenience, that the principal axes of the tensor coincide with those of the crystal and the rotational axis is in the c direction as shown in Fig.3.6. We will then write the following useful formulas:[31-33] for an oblate spheroid, $a = b > c$ and $m = a/c$,

$$D_a = D_b = \frac{1}{2(m^2-1)}\left(\frac{m^2}{(m^2-1)^{1/2}}\arccos\frac{1}{m} - 1\right) \tag{3.10a}$$

$$D_c = \frac{m^2}{(m^2-1)}\left(1 - \frac{1}{(m^2-1)^{1/2}} \arccos\frac{1}{m}\right) \tag{3.10b}$$

where the subscripts (a, b, and c) indicate the corresponding crystallographic directions; for a prolate spheroid, a = b < c and m = c/a,

$$D_c = \frac{1}{m^2-1}\left(\frac{m}{2(m^2-1)^{1/2}} \ln \frac{m + (m^2-1)^{1/2}}{m - (m^2-1)^{1/2}} - 1\right) \tag{3.11a}$$

$$D_a = D_b = \frac{m^2}{2(m^2-1)}\left(1 - \frac{1}{2m(m^2-1)^{1/2}} \ln \frac{m + (m^2-1)^{1/2}}{m - (m^2-1)^{1/2}}\right) \tag{3.11b}$$

A useful relationship that can be shown to exist between the demagnetization coefficients is[31]

$$D_a + D_b + D_c = 2D_a + D_c = 1 \tag{3.12}$$

where $D_a = D_b$ for both special cases.

In practice, samples of cylindrical and disc shapes are usually treated as the limit of prolate and oblate spheroids, respectively.

Since the demagnetization factors are important in the analysis of low field magnetization measurements, we have made many efforts to determine them experimentally. Our first attempt is to find out a proportionality constant related to the flux-signal coupling factor Γ, and then obtain a simple relationship between the SQUID output V_s and the demagnetization factor D. From (3.8), the output signal in a pick-up coil of N turns is

$$V_s = \Gamma\phi = \Gamma\frac{2\pi NVH_a\chi}{R(1+4\pi D\chi)} \tag{3.13}$$

This holds whenever the dipole approximation is appropriate. Define $U = V_s/H_aV$, $\delta = \chi/\chi_0$ (where $\chi_0 = -1/4\pi$ is the susceptibility for complete Meissner effect), and $C = 2\pi N\chi_0\Gamma/R$, the instrumental constant. Then by rearranging (3.13), we have

$$\frac{U(1-\delta D)}{\delta} = C \tag{3.14}$$

Consider at low temperature ($T \approx 0$ K), a calibration sample which has magnetic susceptibility $\chi = \chi_0 = -1/4\pi$ ($\delta = 1$), volume V_0, and a known demagnetization factor D_0, along a crystallographic axis. The SQUID output is V_{s0} in an applied field H_{a0} parallel to the particular crystal direction. (3.14) in this special case reduces to

$$U_0(1-D_0) = C \tag{3.15}$$

This shows that the instrumental constant C can be determined by calibration.

In order to find the value of C, short pieces of superconducting niobium wires of diameters 0.003" (Fine Wire Inc.) and 0.005" (Supercon Inc.), together with a cylindrical lead sample, were used as the standard samples whose demagnetization coefficients were presumably close to the ideal ones of prolate ellipsoids. Some characteristics of those calibration samples are given in Table 2. As can be seen, the flux fill factors of the cylinders differ from that of the dipole by at most 1%, which allows a dipole approximation. The radiuses of the cylinders are much larger than the penetration depth at zero temperature, suggesting $\chi \approx \chi_0 = -1/4\pi$. The average output signal per unit field in the crystallographic c direction, $(V_s/H_a)_c$, was taken from the slope of the V_s-H_a curve.* The volumes of the samples were obtained from the mass and density.

The average value of the proportionality constant C has an uncertainty of about

* The detailed discussions of DC magnetization measurement are given in the following subsection and in Chapter 5.

Table 2. The characteristics of the calibrating Nb and Pb cylinders

Sample	d (Diameter)	ℓ¥ (Length) (mm)	$m = \ell / d$	V (Volume) (10^{-3} mm^3)	R / r‡	2R / ℓ	$2\lambda_0/d$# (10^{-3})	$f_{cylinder}$ (Flux fill factor)	f_{dipole}	Δ*
Nb 1	0.005"	1.28	10.05	16.41	55	6	0.7	0.122	0.124	1%
Nb 2	0.003"	1.47	19.24	6.690	92	5	1.2	0.138	0.140	1.3%
Nb 3	0.003"	1.42	18.69	6.490	92	5	1.2	0.134	0.135	1.2%
Pb 1†	0.0072"	1.26	6.920	22.49	39	6	0.4	0.119	0.121	1%

† The mass of the Pb cylinder is 0.2564 mg.

¥ The lengths of the cylinders were measured from the SEM photographs.

‡ R ~3.5mm is the radius of the pick up coil and r that of the cylinder.

λ_{0Pb} (~ 390 Å) and λ_{0Nb} (~ 440 Å) are the penetration depths at zero temperature.[34]

* Δ is defined as the relative difference between $f_{cylinder}$ and f_{dipole}.

Table 3. Determination of the instrumental constant C by calibration with the Nb and Pb cylinders.

Sample	$(V_s/H_a)_c$* (Volt·Oe^{-1})	$U_c = V_s/H_aV$ (Volt·Oe^{-1}·mm^{-3})	$C = U_c(1-D_c)$ (Volt·Oe^{-1}·mm^{-3})	C (Ave.)
Nb 1	1.047	63.81	63 ± 2	
Nb 3	0.430	66.24	66 ± 1	64 ± 1
Pb 1	1.510	67.14	65 ± 1	

* The V_s's are measured with a sensitivity setting of the SHE control unit of × 10.

2 %, see Table 3, which may result from misalignment of the sample with respect to the applied magnetic field or inaccuracy of volume estimation. In any event, more dedicated measurements may be required.

Assuming C is known, by measuring $\delta = \chi/\chi_0$ and $U = V_s/H_aV$, we can derive the demagnetization factor D from (3.14), together with (3.12),

$$D = \frac{1}{\delta} - \frac{C}{U} \tag{3.16}$$

In another experimental approach, we form the ratio α (defined to be always ≥ 1) of the SQUID flux signals in fields parallel and perpendicular to the rotational axis of the sample, and combine it with (3.12) and (3.14) to get a simple expression of D in terms of α and δ. We have, for a prolate spheroid (cylinder), $\alpha = V_s{}^a/V_s{}^c$,

$$D_a = \frac{\alpha/\delta_a + 1 - 1/\delta_c}{\alpha + 2} \tag{3.17a}$$

$$D_c = \frac{2/\delta_c - 2\alpha/\delta_a + \alpha}{\alpha + 2} \tag{3.17b}$$

In the special case of our calibrating cylinder samples, $\delta \approx 1$ and (3.17) reduces to

$$D_a = \frac{\alpha}{\alpha + 2} \tag{3.18a}$$

$$D_c = \frac{2 - \alpha}{\alpha + 2} \tag{3.18b}$$

For an oblate spheroid (layered crystal), $\alpha = V_s{}^c/V_s{}^a$, we find

Table 4. Demagnetization factors of Nb cylinders determined by the SQUID signal ratio method

Sample	$V_s^{c\dagger}$ (Volt)	$V_s^{a\dagger}$ (Volt)	α^*	D_a			D_c		
				Measured	Calculated	$\Delta^\ddagger$	Measured	Calculated	$\Delta^\ddagger$
Nb 1	1.018	1.931	1.896	0.487	0.490	0.7%	0.027	0.020	26%
Nb 2	0.428	0.828	1.936	0.492	0.496	0.9%	0.016	0.007	56%
Nb 3	0.436	0.862	1.978	0.497	0.496	0.2%	0.006	0.008	26%

† The sensitivity setting of the SHE unit was × 10.

* $\alpha = V_s^a / V_s^c$ and the V_s´s were taken in field H_a = 1 Oe.

‡ Δ is the relative difference between the measured and calculated values.

$$D_a = \frac{1/\delta_a + \alpha - \alpha/\delta_c}{2\alpha + 1} \tag{3.19a}$$

$$D_c = \frac{2\alpha/\delta_c - 2/\delta_a + 1}{2\alpha + 1} \tag{3.19b}$$

As shown in Table 4, the agreement between the measured and the calculated values is good for D_a (< 1%) but poor for D_c, since D_c is already vanishingly small. A comparison of the two experimental methods will be made for the Bi-2212 single crystals in Chapter 5.

3.3.3 DC Magnetization

Following is the typical experimental procedure for low field DC magnetization measurements: first, cool the sample down to the liquid helium temperature in zero field, referred to as "Zero Field Cooled" (ZFC), then apply a static magnetic field as described in 3.2.2 and start to warm the sample up by supplying a current to a heater either at a constant rate (typically ~2.5° per minute) with a Ramp Generator or at a rate controlled manually with a Heater Drive; in the mean time, pump out the helium gas from the sample space with a diffusion pump to maintain a vacuum of about 10^{-4} torr. A curve of a typical zero field cooled run for a Bi-2212 single crystal is shown in Fig. 3.7. If the sample is cooled through the transition in the presence of an applied magnetic field, the process is then referred to as "Field Cooled" (FC) and a field cooled curve is shown also in Fig. 3.7. The field cooled curve does not show the complete flux expulsion and indicates a "Meissner fraction" of about 30%. The incomplete shielding is mainly from the flux trapping by crystal defects. The output signals are recorded by a computer via interface electronics.

3.3.4 AC Susceptibility

The measurement of the complex AC susceptibility, $\chi = \chi' + i\chi''$, can be carried out simultaneously with the DC magnetization measurement. The variations of χ' and χ'' with temperature are illustrated in Fig. 3.8. The profile of the real part of susceptibility χ' is seen to be similar to that of the DC magnetization. In contrast, the imaginary component χ'' has a sharp peak near the transition temperature where χ' changes most rapidly. The out-of-phase component of AC susceptibility is related to energy losses, due to the delaying response of the sample to the AC magnetic field. Because of this, the complex susceptibility is useful in analyzing the dynamic process involving energy dissipation, for example, of flux motion in single crystals.

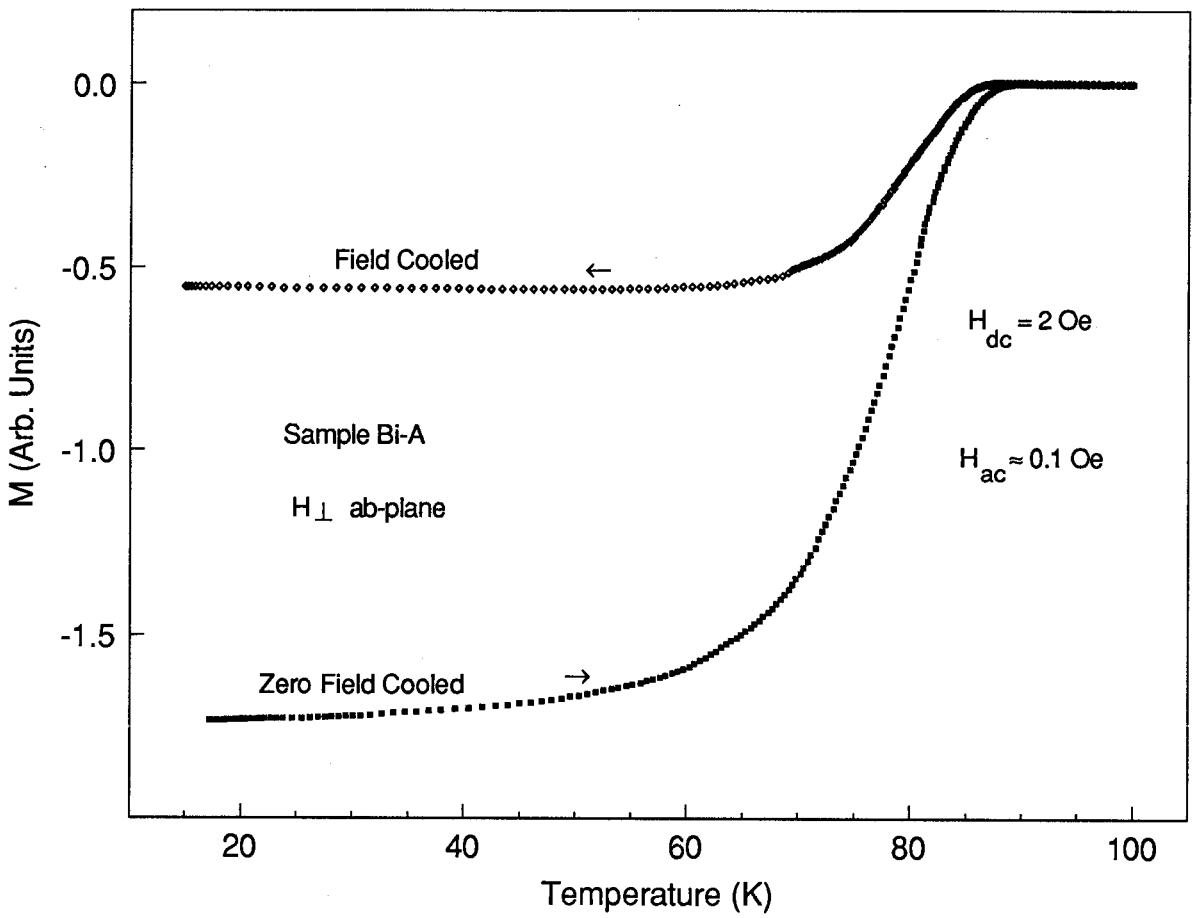

Fig. 3.7. Temperature dependent zero field cooled and field cooled magnetizations of Sample Bi-A in a DC field of 2 Oe and an AC field of 0.1 Oe (amplitude). The field is perpendicular to the ab-plane.

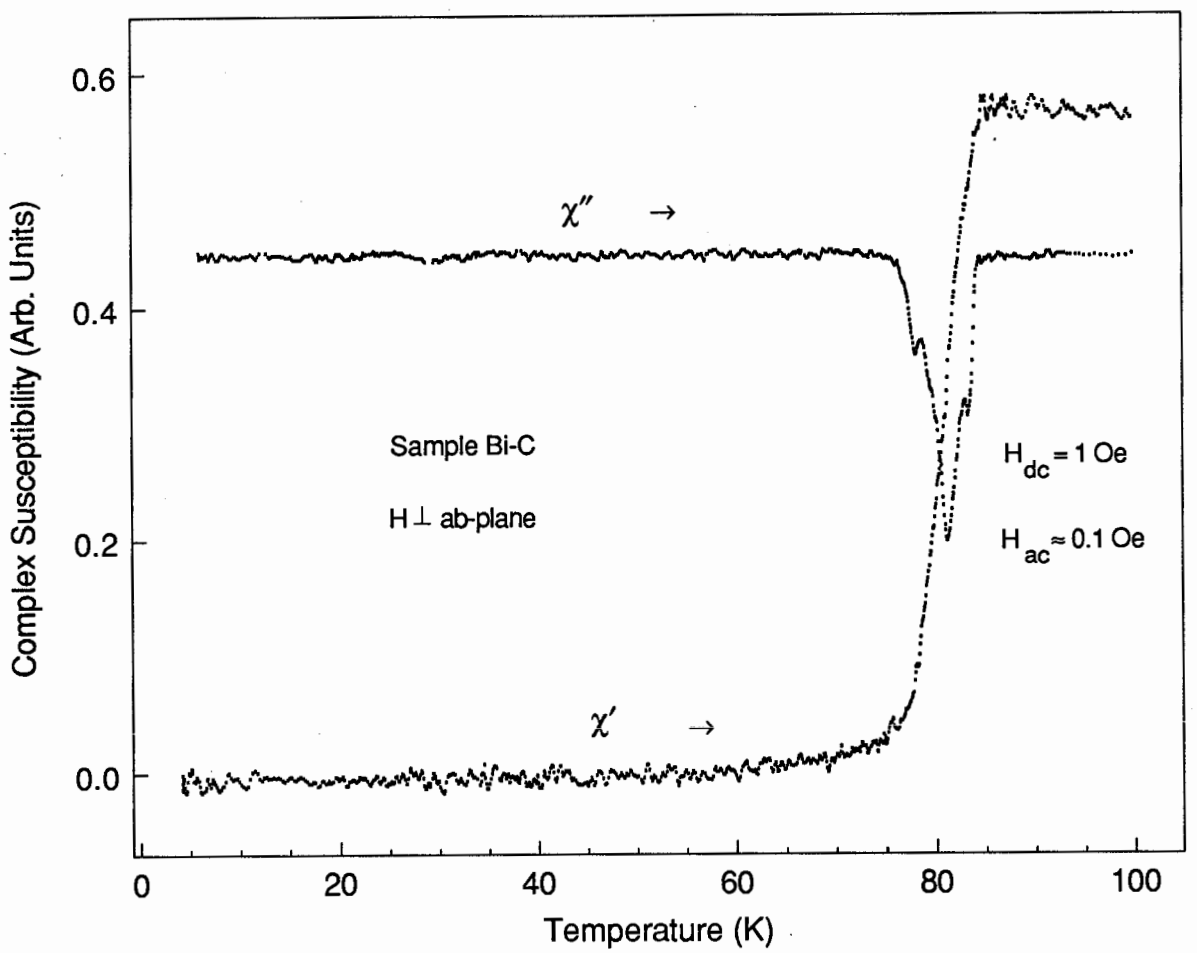

Fig. 3.8. The complex susceptibility of Sample Bi-C in a DC field H_a = 1 Oe and an AC field of 0.1 Oe (amplitude). The fields are perpendicular to the ab-plane.

Chapter 4 Results and Discussions

Thanks to the high sensitivity of the SQUID magnetometer, the DC magnetizations in low magnetic fields of small $Bi_2Sr_2Ca_1Cu_2O_8$ single crystals are measured. The deviations from the linear response to the applied field are regarded as the thresholds of the lower critical fields after the demagnetization factors have been taken into account. The best fit to the measured magnetic flux penetration is obtained with a prediction of the BCS theory and gives an estimate of the penetration depth at zero temperature. The interpretation of the complex magnetic susceptibility measurement requires an understanding of flux motion in the new high-T_c superconductors. Those are the main tasks of this thesis as well as the outlines of this chapter.

4.1 Determination of Lower Critical Fields

4.1.1 Demagnetization Factors

We simply follow the procedures and approaches described in Section 4.3 to determine the demagnetization coefficients for our single crystals. The geometrical characteristics of the two selected crystals, Bi-H and Bi-I, are listed in Table 5. The crystals were weighed with an electrobalance (CAHN G-2), their average thickness was estimated from the SEM images, and their density was obtained from the energy dispersive x-ray spectroscopy. The flux fill factor of the crystals, $f_{crystal}$, deviates from that of a dipole, f_{dipole}, by at most 0.6% as shown in Table 5, which again suggests that a dipole approximation is appropriate. The SQUID output signal per unit field and volume was obtained from the initial slope of the V_s-H_a curve. We will again use the notations, $\parallel$ (a or b direction) and $\perp$ (c direction), to describe the quantities parallel and perpendicular to the crystal basal plane respectively. We found, through the measurement of magnetic penetration depth to be discussed in Sec. 5.2, for our Bi-2212 single crystals:

Table 5. Geometrical characteristics of the $Bi_2Sr_2Ca_1Cu_2O_8$ single crystals

Sample	M Mass (mg)	ρ Density (g/cm^3)	A* Area (mm^2)	r† Radius (μm)	t* Thickness (μm)	$m = 2R/t$	R/r	V Volume (10^{-3}mm^3)	$f_{crystal}$	f_{dipole}	Δ‡
Bi-H	0.021	5.34	0.737	484	5.2	180	7.2	3.97	0.0005	0.0005	0.6%
Bi-I	0.020	5.34	0.390	352	8.4	73	10	3.74	0.0009	0.0009	0.3%

* The area and the thickness of the samples were estimated from the SEM images.

† The radius is a mean value measured from the SEM photographs.

‡ Δ is the relative difference between $f_{crystal}$ and f_{dipole}.

$$\begin{cases} \delta_{\parallel} = \chi_{\parallel}/\chi_0 < 1 \\ \delta_{\perp} = \chi_{\perp}/\chi_0 \approx 1 \end{cases} \tag{4.1}$$

and $\delta_{\parallel}$ is 0.89 for Bi-H and 0.93 for Bi-I. Thus (3.19) can be reduced to

$$D_{\parallel} = \frac{1}{\delta_{\parallel}} - \frac{C}{U_{\parallel}} \tag{4.2a}$$

$$D_{\perp} = 1 - \frac{C}{U_{\perp}} \tag{4.2b}$$

Because the actual values of $D_{\parallel}$ are very small for those platelet-like crystals, within the experimental uncertainty, (4.2a) always gave unphysical negative values of $D_{\parallel}$. We used the relation (3.12) as well as (4.2b) to obtain the values of both $D_{\perp}$ and $D_{\parallel}$, and the results are summarized in Table 6.

Similarly, taking $\delta_{\perp} = \chi_{\perp}/\chi_0 \approx 1$, (3.17) can be simplified:

$$D_{\parallel} = \frac{1}{\delta_{\parallel}(2\alpha + 1)} \tag{4.3a}$$

$$D_{\perp} = 1 - \frac{2}{\delta_{\parallel}(2\alpha + 1)} \tag{4.3b}$$

and the results of this method are shown in Table 7.

As can be seen from both tables, the agreement between the two experimental methods is good for $D_{\perp}$ to within 0.3%. There is also good agreement between the calculated and measured values to within 1% in either method. The relative differences in $D_{\parallel}$ are much larger as expected, due to the very small values of $D_{\parallel}$.

It is easy to show that the uncertainty in both the susceptibility fraction χ/χ_0 and instrumental proportionality constant C has little influence on values of $D_{\perp}$ in the case of our Bi-2212 crystals. We should point out, however, that it is 1/1-$D_{\perp}$ that will come

Table 6. Demagnetization factors of $Bi_2Sr_2Ca_1Cu_2O_8$ single crystals determined by the SQUID signal proportional constant method*

Sample	V_s/H_a† (Volt·Oe^{-1})		$U_{\parallel}$	$U_{\perp}$ (10^3) (Volt·Oe^{-1}·mm^{-3})	$D_{\parallel}$			$D_{\perp}$		
	$\parallel$	$\perp$			Measured	Calculated	Δ‡	Measured	Calculated	Δ‡
Bi-H	0.181 ±4×10^{-3}	17±1	45±1	4.2±0.3	0.007 ±10^{-3}	0.004	43%	0.985 ±2×10^{-3}	0.991	0.7%
Bi-I	0.216 ±5×10^{-3}	8±1	57±1	2.2±0.3	0.015 ±2×10^{-3}	0.011	30%	0.970 ±4×10^{-3}	0.979	0.9%

* C = 64 ± 1 (Volt·Oe^{-1}·mm^{-3}) and $U = V_s / H_a V$ (Volt·Oe^{-1}·mm^{-3}).

† V_s/H_a is taken from the initial slope of the V_s–H_a curve (linear part) and the signals are measured at the sensitivity of × 10 of the SHE control unit.

‡ Δ is the relative difference between the measured and the calculated values for D.

Table 7. Demagnetization factors of the $Bi_2Sr_2Ca_1Cu_2O_8$ single crystals determined by the SQUID signal ratio method

Sample	α^*	$D_{\parallel}$			$D_{\perp}$			$1/(1-D_{\perp})$
		Measured	Calculated	$\Delta^\dagger$	Measured	Calculated	$\Delta^\dagger$	
Bi-H	93 ± 8	$0.0060 \pm 5\times10^{-4}$	0.0043	28%	0.9880 ± 10^{-3}	0.991	0.3%	84 ± 6
Bi-I	37 ± 1	$0.0142 \pm 4\times10^{-4}$	0.0106	26%	$0.9716 \pm 8\times10^{-4}$	0.979	0.7%	35 ± 1

* $\alpha = V_s^{\perp} / V_s^{\parallel}$ and the V_s's are taken from the ratio of the initial slopes of V_s–H_a curves at the sensitivity of × 10 of the SHE control unit.

† $\Delta = |D_{obs} - D_{cal}| / D_{cal}$.

into the determination of the lower critical fields. In other words, $1/1-D_{\perp}$ can have relatively large uncertainty although the uncertainty in $D_{\perp}$ is small. For example, the typical uncertainty in $D_{\perp}$ is about 0.1%, which leads to the uncertainty of about 8% in $1/1-D_{\perp}$. Therefore, the determination of demagnetization factors with the experimental methods still faces challenges.

The advantage of the ratio method over the proportionality constant one is that there is no need to measure the sample's volume which, for our tiny specimens, is very difficult to measure. Its disadvantage for the very thin layered crystals however, lies in the requirement of the knowledge of the susceptibility fraction χ/χ_0. We can obtain χ/χ_0 independently from the determination of λ (see later). Therefore, the demagnetization factors obtained with the signal ratio method were adopted.

4.1.2 DC Magnetizations

Good crystals were selected with needles under an optical microscope (BAUSCH & LOMB) by cleaving them from large crystals, so that they would appear to have smooth surfaces and no stacking fault. Sample Bi-I was obtained by a subsequent cutting with a razor blade from one of the selected crystals. Fig. 4.1 shows, as an example, three temperature dependent magnetizations, whose magnitudes of the total transition vary with the applied field. The temperature sweeps are from 4.2 K to about 100 K. The critical temperature is 85 K for Bi-H and 87 K for Bi-I. In the zero field cooled cycling, the applied magnetic field was started as low as 0.1 Oe and increased to about 1 Oe with a field increment of 0.1 Oe; the field was then increased to about 5 Oe in steps of 0.5 Oe and then to about 10 Oe in steps of 1 Oe; after that a few field points were scattered between 10 Oe and 100 Oe, the highest DC field available. Recording the DC SQUID signals (the transition heights) against the applied fields, we obtained the DC magnetization curves at 4.2K.

To check the operational linearity of the SQUID magnetometer, similar DC magnetization measurements were carried out for several conventional (low T_c)

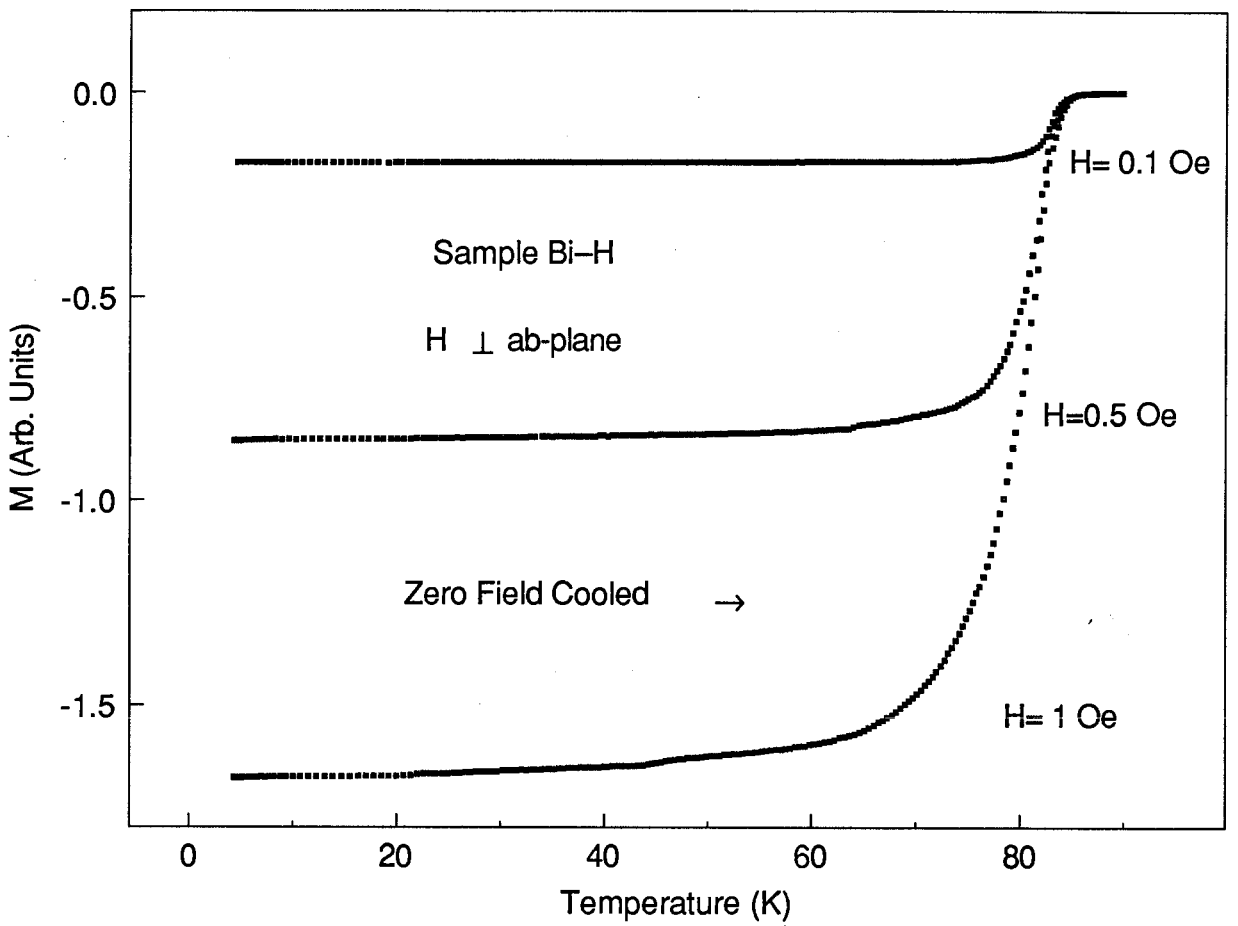

Fig. 4.1. Temperature dependent zero field cooled magnetizations of Sample Bi-H in perpendicular DC fields of 0.1, 0.5, and 1 Oe.

superconductors. Three samples, a lead slab (~ 1×1 mm^2 in size and ~ 0.1 mm in thickness), a lead sphere (~ 1.4 mm in radius), and a niobium cylinder (0.127 mm in diameter and ~ 1.3 mm in length) were chosen for the measurement. The values of the critical fields in the literature are: $H_c(4.2K)$ ~ 550 Oe for lead and $H_{c1}(4.2K)$ ~ 1300 Oe for niobium. Those values are much higher than the upper limit of the DC field the SQUID magnetometer can supply. As can be seen in Fig. 4.2, the M-H curve is linear for the lead slab when $H_a < 30$ Oe;* for the lead sphere and the niobium cylinder however, this linearity remains up to $H_a = 100$ Oe.

Fig. 4.3 shows the magnetization curves of Sample Bi-H in both field orientations. The data points were obtained from the transition heights of the M-T curves. The solid lines were extrapolated from the initial points by first order least-square fitting for very small applied fields ($H_a \leq 1$ Oe). Without considering the demagnetization effect, we can see the bending of the curves in both field configurations except that the curve in parallel fields breaks away more prominently than the one does in perpendicular fields. After the subtraction of the data points from the corresponding points along the straight line, the breakaways can be seen more clearly (see Fig. 4.4) and appear at 2.2 ± 0.2 Oe in the parallel field and 1.8 ± 0.2 Oe in the perpendicular field. With the application of the same procedure to Sample Bi-I, we have observed similar magnetization profiles as shown in Figs. 4.5 and 4.6, from which we located the breakaways to be at 3 ± 0.2 Oe in the parallel field and 2 ± 0.2 Oe in the perpendicular field.

* The too early deviation may result from the deformation in the crystal when the lead sample was rolled into a thin slab.

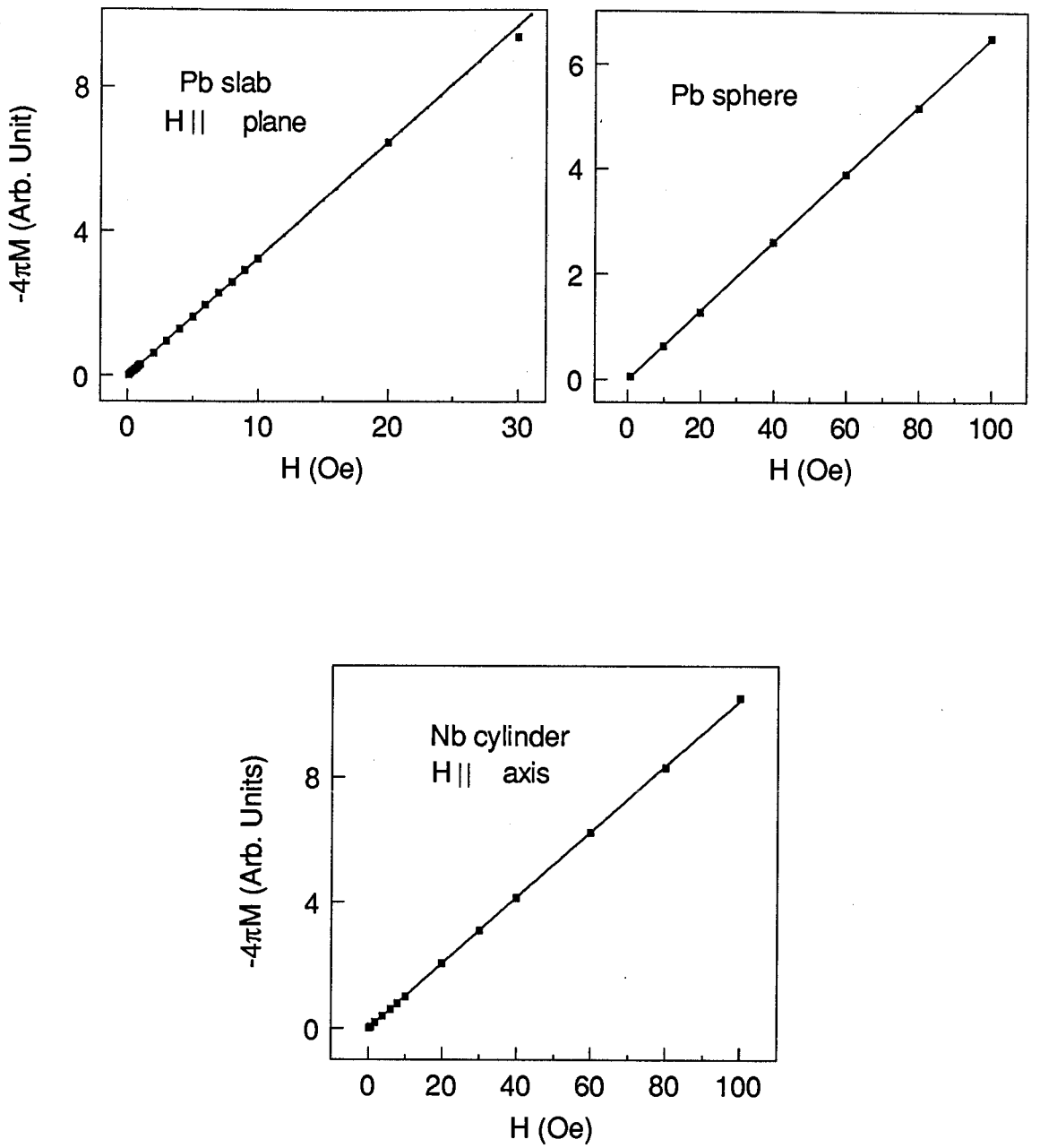

Fig. 4.2. Magnetization curves of a lead slab, a lead sphere (upper), and a niobium cylinder (lower) with no demagnetization correction applied.

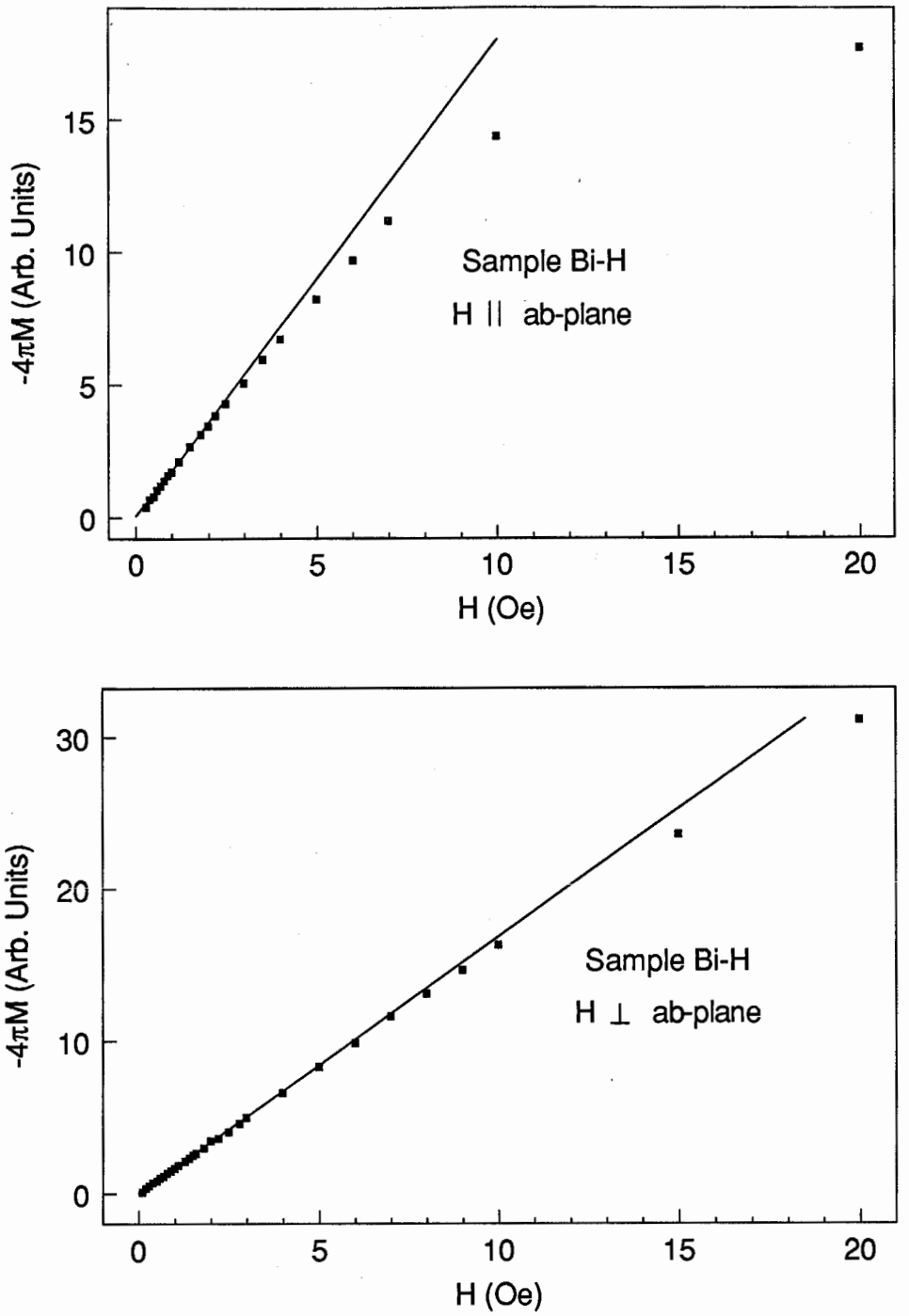

Fig. 4.3. Magnetization curves of Sample Bi-H determined from the transition heights of M–T curves in the applied fields parallel (upper) and perpendicular (lower) to the ab-plane without demagnetization corrections. The solid lines are linear fits to the low field points.

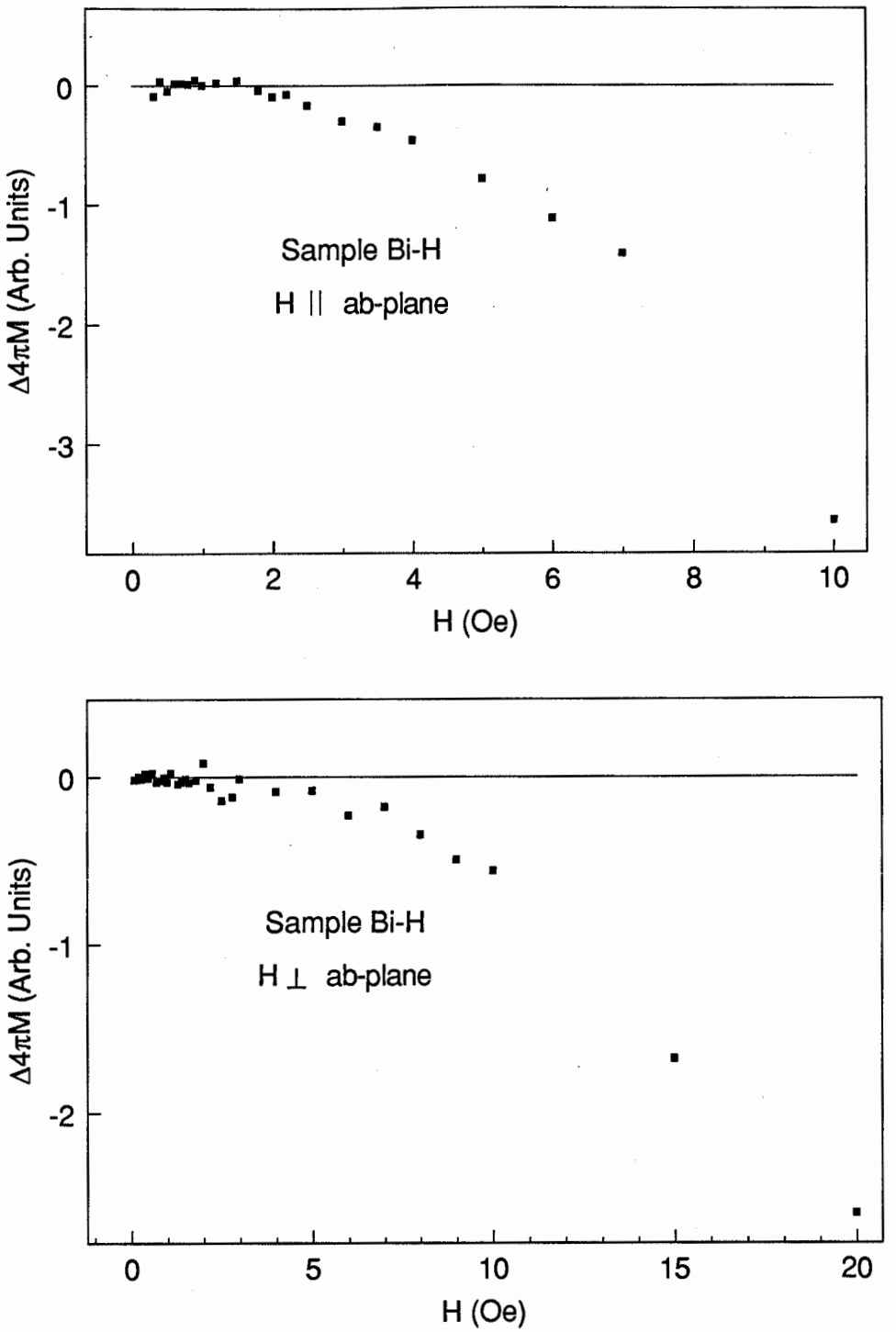

Fig. 4.4. Deviation of the magnetization from the linear increase in low fields for Sample Bi-H. No demagnetization correction is applied. The applied fields are parallel (upper) and perpendicular (lower) to the ab-plane.

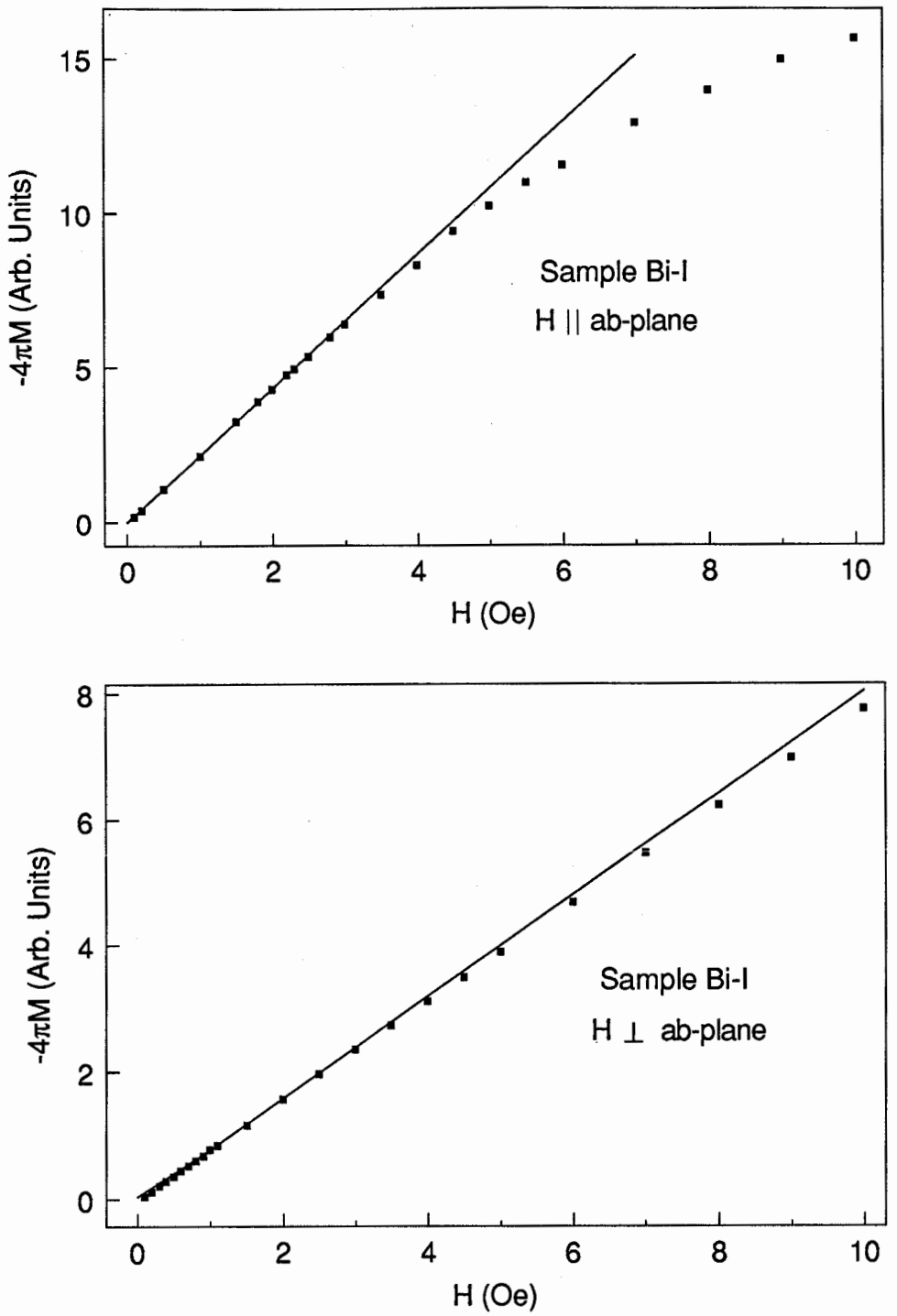

Fig. 4.5. Magnetization curves of Sample Bi-I determined from the transition heights of M–T curves in the applied fields parallel (upper) and perpendicular (lower) to the ab-plane without demagnetization corrections. The solid lines are linear fits to the low field points.

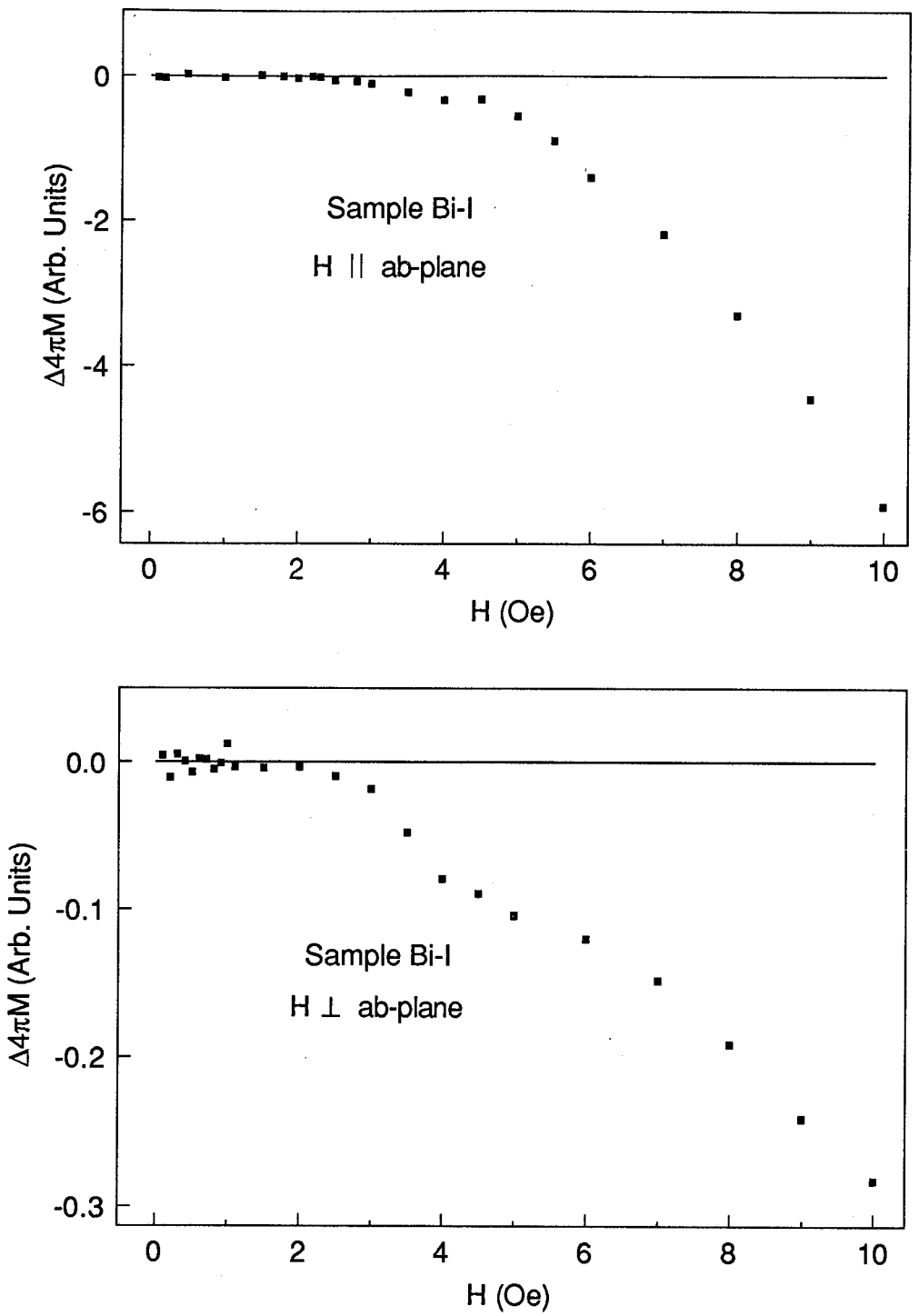

Fig. 4.6. Deviation of the magnetization from the linear increase in low fields for Sample Bi-I. No demagnetization correction is applied. The applied fields are parallel (upper) and perpendicular (lower) to the ab-plane.

4.1.3 Lower Critical Fields

By convention, we interpret the breakaways seen in the magnetization curves to be the onsets of the flux penetration into the crystals. Thus, the lower critical fields can be determined from the relation

$$H_{c1} = \frac{H_{a0}}{1 + 4\pi\chi D} \tag{4.4}$$

where H_{a0} corresponds to the applied field or entrance field where the magnetization curve starts to deviate from the initial straight line. The in-plane demagnetization factors shown in Tables 6 and 7 basically approach zero, so the internal field of the sample is approximately equal to the external field. Whereas the out-of-plane demagnetization factors are large and hence crucial in the determination of the lower critical fields. We take $\chi_{\perp} \approx -1/4\pi$, and (4.4) reduces to

$$H_{c1}^{\perp} = \frac{H_{a0}^{\perp}}{1 - D_{\perp}} \tag{4.5}$$

Summarized in Table 8, the results for our Bi-2212 single crystals at T = 4.2 K show: $H_{c1}^{\parallel} = 2.2 \pm 0.2$ Oe and $H_{c1}^{\perp} = 149 \pm 21$ Oe for the uncut crystal (Bi-H); $H_{c1}^{\parallel} = 3 \pm 0.2$ Oe and $H_{c1}^{\perp} = 70 \pm 7$ Oe for the cut crystal (Bi-I). Consequently, the lower critical field anisotropy is 68 ± 11 for Bi-H and 23 ± 3 for Bi-I. We think the large discrepancy in $H_{c1}^{\perp}$ for the two crystals lies in the fact that Sample Bi-I has rough edges because of cutting, which may result in some effects like the large local demagnetization factor and hence an earlier entry of the external field into the crystal. Therefore, the uncut crystal Bi-H is of better quality and its measured values of the lower critical fields should represent intrinsic properties more closely.

Table 8. Experimental estimates of the lower critical fields of the $Bi_2Sr_2Ca_1Cu_2O_8$ single crystals

Sample	H_{a0}* Entrance Field (Oe)		$\frac{1}{1 - D_\perp}$	H_{c1} (Oe)		$H_{c1}^\perp / H_{c1}^{\parallel}$
	$\parallel$	$\perp$		$\parallel$	$\perp$	
Bi-H	2.2 ±0.2	1.8 ±0.2	83 ±7	2.2 ±0.2	149 ±21	68 ±11
Bi-I	3.0 ±0.2	2.0 ±0.2	35 ±1	3.0 ±0.2	70 ±7	23 ±3

* H_{a0} was determined from the breakaway in the M-H curve.

In comparison, the values of the lower critical fields at 4.2 K for $YBa_2Cu_3O_{7-\delta}$ single crystals are:[35] $H_{c1}^{\parallel} \approx 120$ Oe and $H_{c1}^{\perp} \approx 690$ Oe. Thus, the $Bi_2Sr_2Ca_1Cu_2O_8$ single crystals have much lower values but larger anisotropy in the lower critical fields.

J. T. Lin et al. at University of Virginia and M. A. Subramanian et al. at du Pont[36] estimated $H_{c1}^{\parallel} \leq 4$ Oe and $H_{c1}^{\perp} \leq 100$ Oe at $T \approx 7$ K with the DC magnetization measurement on Bi-2212 single crystals. Moreover, G. Shaw et al.[37] at University of Maryland obtained $H_{c1}^{\parallel}$ (4.2 K) ≤ 10 Oe for a magnetization measurement. Apparently, our measurement of $H_{c1}^{\parallel}$ is fairly comparable to both of these results.

L. Krusin-Elbaum et al.[38] at IBM Thomas J. Watson Research Center analyzed the temperature dependent magnetization to determine the onset of the flux penetration, and the low temperature H_{c1} values were determined: $H_{c1}^{\parallel} \sim 80$ - 140 Oe. However, as they pointed out, this method may not probe the H_{c1} boundary but another one in the H-T plane, for example, vortex entanglement or crossover to vortex plasma above H_{c1}.[38] Furthermore, B. Batlogg et al.[39] at AT&T Bell Laboratories found low temperature $H_{c1}^{\parallel}$ values as high as 170 Oe. The large discrepancies for different research groups and laboratories make the determination of H_{c1} of Bi-2212 single crystals a controversial topic.

This should perhaps not be too surprising when one takes a close look at the morphologies of the Bi-2212 single crystals. The commonly observed phenomena, such as stacking faults, intergrowths between the planes, and exfoliations of the layers may result in an earlier penetration of the flux into the sample. On the other hand, the surface barrier owing to the existence of pinning centers, tends to delay the flux entry. The values of the lower critical fields of Bi-2212 single crystals reported so

far, are most probably sample dependent. Obviously, it is desirable to have single crystals of better quality in order to reduce these effects to a minimum.

Pointed out by A. K. Grover et. al.,[40] the determination of H_{c1} may also be affected by the accuracy to which the magnetization is measured. According to Bean's critical state model, for a large slab,

$$-4\pi M \approx H_a - H_a^2/2H^* \qquad H_{c1} << H_a \leq H^* \tag{4.6}$$

where $H^* = \pi J_c D/5$, and J_c (in units of A/cm^2) is the critical current density and D the thickness of the specimen. H^* is the characteristic field that must be applied in order for the flux to completely penetrate into the specimen. A rough estimate indicates that the non-linear term in (4.6) is of the order of 0.1 Oe. Thus for this small deviation from the linear relation, the values of H_{c1} could be overestimated.

4.2 Magnetic Penetration Depth

4.2.1 Normalized Flux

By measuring the low field magnetization or magnetic susceptibility, one observes the variations of those quantities with temperature due to flux penetration. For an infinite large plate of thickness 2a comparable with the dimension of the penetration depth λ in a uniform field H_a parallel to the surface, the internal field can be obtained by solving London's equations. The real part of the magnetic susceptibility can thus be written as[41]

$$\frac{\chi(T)}{\chi_0} = 1 - \frac{\lambda(T)}{a} \tanh \frac{a}{\lambda(T)} \tag{4.7}$$

where $\chi(T) = M/H_a$ (or dM/dH_a in the AC field) is the sample's susceptibility at temperature T and $\chi_0 = -1/4\pi$ is the bulk susceptibility (no field penetration).

Recall that the flux in the pick-up coil is (3.13):

$$\phi(T) = \frac{2\pi NV\chi(T)H_a}{R[1+4\pi\chi(T)D]} \tag{4.8}$$

We now define the normalized flux

$$\alpha = \frac{\phi - \phi_0}{\phi_n - \phi_0} = \begin{cases} 0 & T \approx 0 \\ 1 & T \geq T_c \end{cases} \tag{4.9}$$

where ϕ_0, ϕ_n, and ϕ are the flux at initial ($T \approx 0$), normal ($T \geq T_c$), and arbitrary state respectively, shown in Fig. 4.7. For superconducting samples, the paramagnetism of the normal state is negligible compared with the diamagnetism of the superconducting state. Therefore $\phi_n/\phi_0 \approx 0$ and (4.9) becomes

$$\alpha = 1 - \frac{\phi}{\phi_0} = \begin{cases} 0 & T \approx 0 \\ 1 & T \geq T_c \end{cases} \tag{4.10}$$

Combining (4.7) - (4.10) and noticing that $D_{||} \approx 0$, we can then write an expression for the normalized flux in the more concrete form:

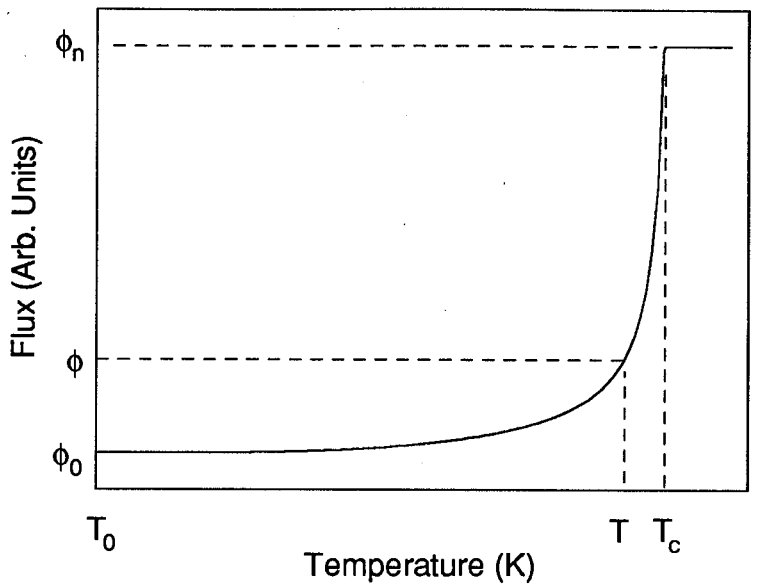

Fig. 4.7. The magnetic flux ϕ_0, ϕ_n, and ϕ at $T \approx 0$, $T \geq T_c$, and arbitrary temperature T.

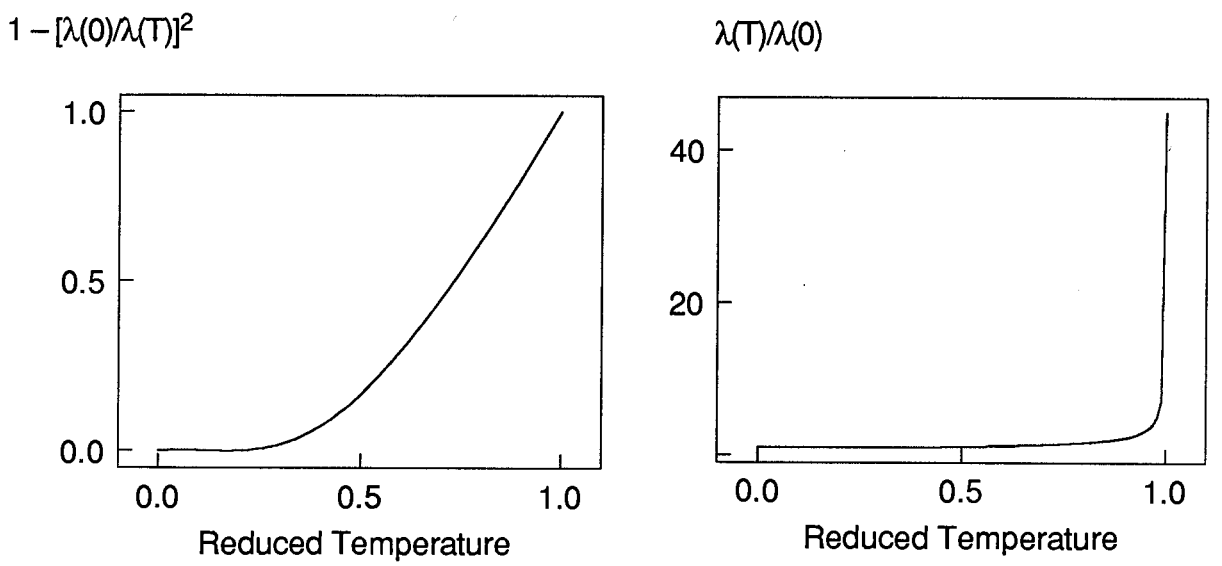

g. 4.8 The clean local limit weak-coupled BCS temperature dependent penetration
epth

$$\alpha(T) = 1 - \frac{\chi(T)}{\chi(0)} = \frac{\frac{\lambda(T)}{a}\tanh\frac{a}{\lambda(T)} - \frac{\lambda(0)}{a}\tanh\frac{a}{\lambda(0)}}{1 - \frac{\lambda(0)}{a}\tanh\frac{a}{\lambda(0)}}$$

$$= \frac{\frac{\lambda(T)}{\lambda(0)}\frac{\lambda(0)}{a}\tanh\frac{a}{\lambda(0)}\frac{\lambda(0)}{\lambda(T)} - \frac{\lambda(0)}{a}\tanh\frac{a}{\lambda(0)}}{1 - \frac{\lambda(0)}{a}\tanh\frac{a}{\lambda(0)}} \qquad (4.11)$$

where $\chi(0)$ and $\lambda(0)$ are the susceptibility and penetration depth at zero temperature, and a the half thickness of the plate. Obviously, the temperature dependence of α comes from $\lambda(T)/\lambda(0)$ with $a/\lambda(0)$ as a parameter.

4.2.2 Comparison with Theory

The mean-field BCS theory gives an expression for the temperature dependence of λ:

$$\lambda(T)^2 = \lambda(0)^2\left(1 - \frac{\partial \ln\Delta(T)}{\partial \ln T}\right) \qquad (4.12)$$

where $\Delta(T)$ is the superconducting gap. This expression was evaluated and tabulated by Muhlschlegel (see plots in Fig. 4.8),[42] assuming a clean local limit and a weak-coupling ratio $2\Delta(0)/kT_c = 3.53$, here $\Delta(0)$ is the superconducting energy gap at T = 0 K. The empirical two-fluid (Gorter-Casimir) model gives:

$$\lambda(T)/\lambda(0) = \left[1 - \left(\frac{T}{T_c}\right)^4\right]^{-1/2} \qquad (4.13)$$

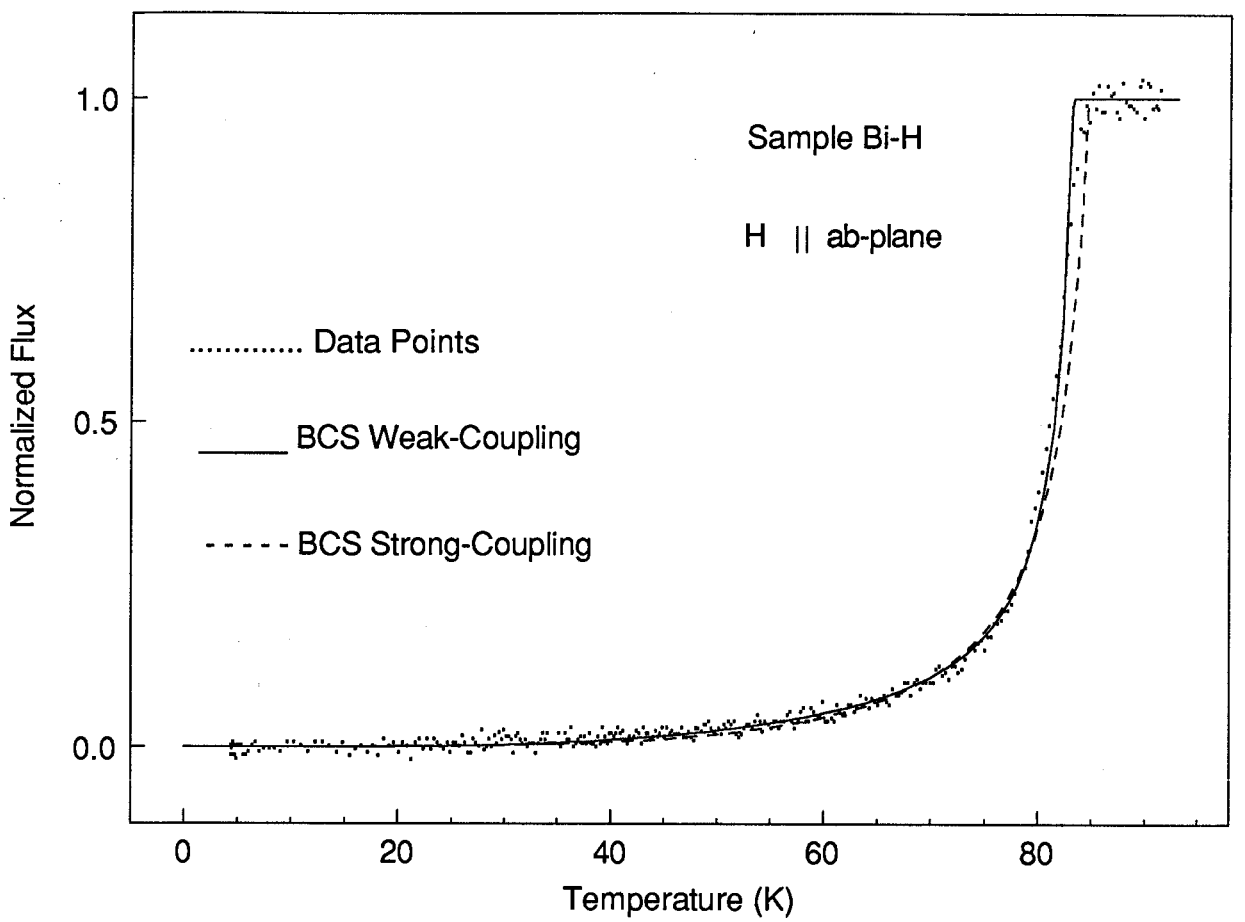

Fig. 4.9. Normalized flux vs temperature for Sample Bi-H. The dots are the experimental data. The solid line is a two-parameter fit with the weak-coupling BCS model and the dashed line that with the two-fluid model (BCS strong-coupling limit).

This relation is believed to closely follow the penetration depth for a strong-coupling BCS superconductor.[43] Substituting the temperature dependence of λ into (4.11) and using T_c, the critical temperature as an additional parameter, we then obtain the expression for the normalized flux with either theoretical model.

The comparison of the experimental data with the theoretical models is achieved by using a least-square two-parameter fitting computer program. As can be seen in Fig. 4.9, the weak-coupling BCS theory appears to give a somewhat better fit. The parameters for the best fit for Sample Bi-H turned out to be $a/\lambda(0) \approx 9.15$ and $T_c \approx 82.5$ K. Knowing the average thickness ($a \approx 2.95$ μm), we estimated the zero temperature penetration depth $\lambda(0) \approx 2900$ Å, note here $\lambda(0) = \lambda_{||}(0)$. Applying the same fitting procedure to Sample Bi-I, we obtained an equally good fit but a much larger value of $\lambda(0)$ (~ 9000 Å). This indicates that the field can penetrate into the cut crystal more easily.

Unlike the case of $Y_1Ba_2Cu_3O_{7-\delta}$ high-T_c superconductors, so far there are few published papers devoted to the study of the magnetic field penetration for $Bi_2Sr_2Ca_1Cu_2O_8$ cuprates. S. Mitra, J. H. Cho, W. C. Lee, D.C. Johnston, and V. G. Kogan[44] at Ames Laboratory and Iowa State University have made a series of investigations of magnetic field penetration for several high-T_c copper oxide superconductors including Bi-2212 single crystals. According to the calculations[44,45], the magnetization in the intermediate range, $H_{c1} \ll H_a \ll H_{c2}$, has a linear relation with the logarithm of the applied field. Their temperature dependent penetration depth is determined from the M(H) isotherm and follows the BCS weak-coupling prediction in the clean local limit. The zero temperature penetration depth $\lambda(0)$ is estimated to be about 3000 Å. Our estimation of $\lambda(0)$ and the temperature dependence of $\lambda(T)$ are thus in good agreement with this measurement.

Muon-Spin-Relaxation (μSR) technique has been extensively used to estimate the magnetic field penetration depth λ of high-T_c superconductors. At this time and for the

Bi-2212 compound, few published μSR results are available. E. J. Ansaldo et. al.[46] performed μSR measurements for a powder sample of Bi-2212 (T_c = 72 K) and found an averaged penetration depth at zero temperature $\lambda(0) \approx 3000$ Å.

Because the temperature dependence of λ is explicitly related to the superconducting energy gap (4.9), the measurement of λ thus provides information regarding the symmetry of the superconducting state and the pairing mechanism. Our temperature dependence of λ has been seen to be more consistent with the prediction of the clean local weak-coupling BCS theory (s-wave pairing). This appears to be a common feature, derived from many experimental measurements with different techniques for both Y-123[44,47-50] and Bi-2212 high temperature superconductors.

At this point, we are still not certain whether the large value of $\lambda(0)$ is due to the stacking faults and/or the inhomogeneities in the crystal or an intrinsic property. As pointed out by many authors, the absolute magnitude of $\lambda(0)$ cannot be determined unambiguously by any fitting procedure without prior knowledge of the correct theory for the temperature dependence of $\lambda(T)$.

The zero temperature penetration depth $\lambda(0)$ can be used to estimate the carrier density. If we assume the conventional London formula[41]

$$\lambda(0) = [m^* c^2/4\pi n e^2]^{1/2} \qquad (4.14)$$

where n is the normal-state carrier density and m^* the effective mass of the carriers, e is the electron charge and c the speed of light, in c.g.s. units, then taking $\lambda(0) \approx 2900$ Å, we obtain the ratio n/m^* to be of the order of 3×10^{48} carriers/cm^{3}g. This is lower than that of Y-123 single crystals by one order of magnitude. If (as a crude estimate) we take further $m^* \sim m_e$, the electron mass, we find a carrier density of the order of 3×10^{21} carriers/cm^3.

4.3 Energy Dissipation of Flux Motion

The complex susceptibility $\chi = \chi' + i\chi''$ provides information about the flux entry and energy dissipation of flux motion, and its measurement has been performed on our Bi-2212 crystals. In the zero field cooled runs, an AC field, superimposed with a DC field, was applied to the sample. The amplitude of the AC field was a few mG and the frequency was 160 Hz. The DC field was varied between 1 Oe and 100 Oe. The upper part of Fig. 4.10 shows the temperature dependence of the imaginary part of the AC susceptibility in different DC fields for one of our Bi-2212 crystals. The positions of the peaks in $\chi''(T)$ shift to lower temperatures and their magnitudes increase as the field increases.

The correct interpretation of the complex susceptibility measurements relies on the understanding of properties of the flux lattice (Abrikosov lattice) and the state of individual flux lines in single crystals of the high-T_c superconductors. Toward the end of 1986, K. A. Muller, M. Takashige, and J. G. Bednorz[51] of the IBM Zurich Research Laboratory made an observation of the time dependence of nonequilibrium magnetizations in a polycrystalline La-Ba-Cu-O sample and discussed flux motion in single crystals as well as within the grains. In the past year, many experiments have been carried out[52-56] in an attempt to understand the unusual behavior of the new oxide superconductors in the presence of a magnetic field.

According to the critical state theory of Bean, Kim, and Anderson,[57-60] the Abrikosov lattice is formed in a type II superconductor at a field $H_a \geq H_{c1}$, and a current flowing in such a superconductor exerts a "Lorentz force" on the flux lines (fluxons), tending to make them move. Flux motion driven by the Lorentz force is called "flux flow". In "hard" superconductors, the fluxons are pinned to prevent this motion. Pinning is caused by material inhomogeneities, such as point defects or grain boundaries, that make it energetically more favorable for a fluxon to occupy one position than another. To be effective, however, the pinning energy U_0 must greatly

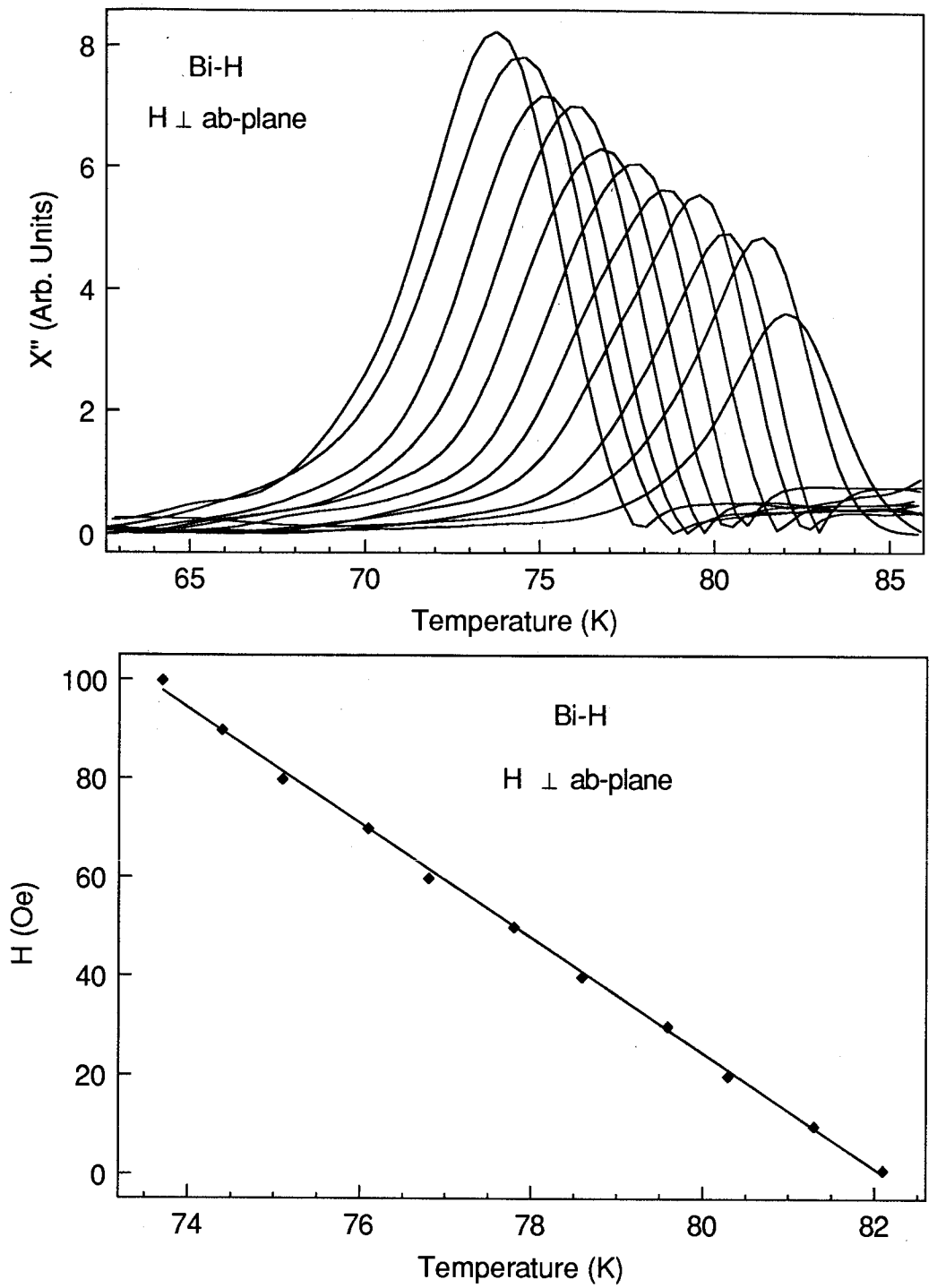

Fig. 4.10. Upper: the temperature dependence of the imaginary part of the AC susceptibility (χ") in various DC fields. Lower: the field dependence of the peak temperature.

exceed the thermal energy kT (where k is Boltzmann's constant), because the probability of thermally activated escape from a pinning center is proportional to $\exp(-U_0/kT)$. Flux motion caused by thermal activation is called "flux creep". For high temperature superconductors, the flux creep is unusually large at temperature and field values at which the Abrikosov lattice is well formed. This may be due to the following two reasons. One is the higher critical temperature of the copper oxide superconductors, which means that there is more thermal energy for flux lines to hop over the energy barriers. The other is the superconductors' large anisotropy and short coherence length, which means that the energy barriers are smaller, because the pinning energy U_0 is proportional to a correlation length L_c (which can be reduced by the large anisotropy) and the G-L coherence length ξ (see, for example Ref. 61).

As pointed out by many researchers,[54,55] there is an "irreversibility line" in the H-T plane of oxide superconductors. Below this line the Abrikosov lattice is disordered and, although pinned to crystal defects, is susceptible to giant flux creep. Above this line, the flux lines can move freely with respect to the crystal lattice. In other words, the zero field cooled and field cooled magnetizations are the same in this region.

In the presence of an AC field, the magnetic flux penetrates the crystal and the Abrikosov vortices sweep in and out of the sample, causing hysteresis losses. The onset of the energy losses seen in $\chi''(T)$ may present the onset of the flux creep and allow, in principle, the determination of the lower critical fields. Because the out-of-phase AC susceptibility measurement is not sensitive enough to detect the initial flux penetration, this onset in our $\chi''(T)$ curve can not be clearly defined. However, the peaks in the $\chi''(T)$ curves provide us a well defined field versus temperature line, as illustrated in the lower part of Fig. 4.10. We speculate that this line is closely related to the irreversibility line in the low field domain. The slope of this line is approximately 0.1 T/K. The magnetic field along the irreversibility line could vary as some power of T_{irr}/T_c (for example, 3/2)[54] for some range of field and temperature values, where T_{irr} is

the irreversibility temperature. Further low DC field magnetization measurements are needed to directly measure the irreversible behavior and confirm this speculation.

Theoretical calculations of the critical state model have been made by many authors, for example J. R. Clem[63] and K. H. Muller,[64] for granular high temperature superconductors. In their arguments, the complex susceptibility measurement at a variety of different fields and temperatures could be used to determine the values and field and temperature dependence of the critical current density $J_c(H,T)$. One thus expects that similar calculations for single crystalline samples should be useful.

4.4 Superconducting Parameters

Having measured the lower critical fields H_{c1}'s and the penetration depth λ at zero temperature, we are now in the position to estimate other fundamental superconducting quantities by employing the formulas developed from the anisotropic Ginzburg-Landau theory.

The anisotropic G-L parameter κ first of all, can roughly be evaluated from (1.5):

$$\kappa_{\perp} \approx \exp\left(\frac{4\pi\,\lambda_{\parallel}^{2}\,H_{c1}^{\perp}}{\phi_0}\right) \qquad (4.15)$$

Using the measured $\lambda_{\parallel}$ (~ 2900 Å) and $H_{c1}^{\perp}$ (~ 149 Oe) values, we estimate $\kappa_{\perp}$ to be of the order of 2×10^3. Since $\kappa_{\perp}$ is determined from an exponential function, it obviously has a large uncertainty.

Combining (1.2) - (1.5), one can derive the following formula in a straightforward manner:[65]

$$\frac{H_{c1}^{\parallel}}{H_{c1}^{\perp}} = \frac{1}{\gamma}\left(1 + \frac{\ln\gamma}{\ln\kappa_{\perp}}\right) \tag{4.16}$$

where $\gamma = (M/m)^{1/2}$. By solving (4.16) numerically with the experimentally observed values of H_{c1} and the above $\kappa_{\perp}$, we estimate the superconducting anisotropy constant γ to be the order of 110. The effective mass ratio is then $\gamma^2 = M/m \sim 1.2\times10^4$. We notice here that γ is insensitive to $\kappa_{\perp}$ because of the logarithmic relation and therefore determined mainly by the anisotropy in H_{c1}.

The effective mass anisotropy has been measured independently by D. E. Farrel et al.[66] with the torque technique. The theoretical basis behind the experiment predicted that the magnetization of the crystal has a transverse component to the applied field.[67-69] This measurement gives a temperature independent γ value of 55.

The upper critical fields can also be used to derive γ through the relation

$$H_{c2}^{\parallel} / H_{c2}^{\perp} = \gamma \tag{4.17}$$

Values of γ measured by this method range from 8 to 143.[70-75] Because of the large flux creeping in the high temperature superconductors, there are increasing concerns about whether the conventional resistivity measurement, from which H_{c2} is usually determined, is probing the equilibrium values. High field magnetic measurements have been carried out[76] to obtain H_{c2} values for Y-123 single crystals. So far there is as yet no such a measurement for Bi-2212 single crystals. Since the upper critical fields are important superconducting quantities, it may be worthwhile to perform the high field magnetic measurements in order to obtain the anisotropy constant γ and evaluate the microscopic parameters like superconducting coherence length and their anisotropy. J. R. Cooper et. al.[77] reported a γ value as large as 550, by measuring the normal state resistivity and using a simple Drude model

$\rho = m^*/ne^2\tau$, where τ is the scattering time. From our measurement and others, the giant effective mass ratio suggests two-dimensional superconductivity. In fact Bi-2212 has the largest superconducting anisotropy ever found for the layered superconducting compounds.[17]

The penetration depth $\lambda_\perp$ is controlled by the shielding current flowing between the Cu-O planes. This is the situation as shown in Fig. 1.2 where the applied field is parallel to the ab-plane. Using the simple relation (1.2a), $\lambda_\perp = \lambda_{||}\gamma$, we estimate $\lambda_\perp \approx 32$ μm. The in-plane dimension (in a or b direction) of the selected crystals is ~ 1 mm which is considerably larger than that of $\lambda_\perp$. Consequently, the change in susceptibility $\chi(T)$ due to this field penetration is negligible. To make the sample size comparable to $\lambda_\perp$, J. R. Cooper et. al.[77] cut a single crystal into a smaller piece and measured the reduced magnetic susceptibility. They obtained a $\lambda_\perp$ value of about 100 μm. This large $\lambda_\perp$ value seems to be another evidence showing the easier field penetration into the cut crystals due to the edge damage.

In a magnetic field above H_{c1}, a hard superconductor will induce a bulk critical current determined by the strength with which flux lines are pinned. The critical current density J_c can be estimated from a magnetic hysteresis measurement and Bean's critical state model. The highest critical current density possible in a superconductor is the "depairing" critical current density, J_{cd}, above which the current delivers sufficient momentum to break up the "Cooper" pairs of electrons that are responsible for superconductivity. For a superconductor at the lower critical field H_{c1}, J_{cd} can be estimated from Maxwell's equations and the approximation:

$$H_{c1}/\lambda \sim dH/dx = (4\pi/c)J_{cd} \qquad (4.18)$$

This limit applies to the surface of the sample to a depth of about λ. Substituting our measured H_{c1} and λ values into (4.18) and expressing the values of J_{cd} in the convenient units (A/cm^2), we have

$$J_{cd\parallel} \sim \frac{5}{2\pi}\frac{H_{c1}^{\perp}}{\lambda_{\parallel}} \approx 4\times10^{6}\,A/cm^{2} \qquad (4.19a)$$

$$J_{cd\perp} \sim \frac{5}{2\pi}\frac{H_{c1}^{\parallel}}{\lambda_{\perp}} \approx 6\times10^{2}\,A/cm^{2} \qquad (4.19b)$$

where $J_{cd\parallel}$ and $J_{cd\perp}$ are the depairing critical current density parallel and perpendicular to the ab-planes respectively, and H_{c1} and λ are in c.g.s. units. The huge anisotropy in J_{cd} indicates that the shielding currents flow much more easily in the Cu-O plane than between the planes. The bulk critical current density J_c estimated with Bean's model in the literature[36,37] is of the order of 10^4 A/cm^2 in the "easy" direction (a or b direction). In comparison, $J_{cd\parallel}$ for Y-123 single crystals[35] is of the order of 10^7 A/cm^2 and $J_{c\parallel}$ of the order of 10^6 A/cm^2.[79,80] The low value of J_{cd} (and J_c) along the "hard" direction (c direction) is expected owing to the giant superconducting anisotropy. Superconductivity in this direction is probably of the Josephson-coupled nature.

Chapter 5 Conclusions

5.1 Summary

1) The $Bi_2Sr_2Ca_1Cu_2O_8$ single crystals were obtained by a flux-growth method. The energy dispersive x-ray spectroscopy gave a cation ratio very close to the ideal composition. The unit cell lattice constant $c \approx 30.81 \pm 0.04$ Å was obtained by indexing the x-ray diffraction patterns. The transition temperatures of the selected crystals, 85 K for Bi-H and 87 K for Bi-I, were obtained from AC susceptibility measurements.

2) We performed low field DC magnetization measurements on two selected single crystals. The lower critical fields at 4.2 K were determined: $H_{c1}^{\parallel} = 2.2 \pm 0.2$ Oe and $H_{c1}^{\perp} = 149 \pm 21$ Oe for the uncut crystal (Bi-H), $H_{c1}^{\parallel} = 3 \pm 0.2$ Oe and $H_{c1}^{\perp} = 70 \pm 7$ Oe for the cut crystal (Bi-I). We believe that the values from the uncut crystal represent more closely the intrinsic properties of good quality samples.

3) The temperature dependence of the magnetic penetration depth $\lambda(T)$ obtained from the measurement of the AC susceptibility, follows the prediction of the weak-coupling BCS theory in a clean local limit, indicating an s-wave pairing mechanism. The two-fluid model does not seem to fit the data quite as well. The penetration depth at zero temperature was determined from a two-parameter least-square fitting procedure and found to be about 2900 Å. This is in good agreement with other recent measurements on Bi-2212 single crystals.[44] The value of $\lambda(0)$, together with the London's formula, implies a carrier density of the order of 3×10^{21} carriers/cm^3.

4) A well defined line in the H-T phase diagram was obtained from the peak position of the imaginary component of the AC susceptibility χ''. We interpret this line to be closely related to the irreversibility line in the low field domain.

5) In the context of the anisotropic Ginzburg-Landau theory, we estimated the G-L parameter $\kappa_{\perp}$ of the order of 2×10^3 and the effective mass ratio $\gamma^2 = M/m$ of the order of 1.2×10^4.

6) Using Maxwell's equations, we estimated the equilibrium supercurrent density (depairing critical current density) $J_{cd\parallel} \sim 4\times10^6 A/cm^2$ and $J_{cd\perp} \sim 6\times10^2 A/cm^2$. This results, together with the giant effective mass ratio, suggests two-dimentional superconducting behavior.

5.2 Suggestions for Future Work

The search for favorable conditions to grow single crystals of Bi-2212 of better quality with a useful size is still a challenging task.

Since it is possible to carry out high field AC susceptibility measurements by using an existing flow-cryostat with a built-in superconducting 5 T magnet, one could obtain the upper critical fields H_{c2} and their anisotropy. This, along with the low field measurement, can be used to obtain more accurate fundamental superconducting parameters, such as the superconducting anisotropy constant γ, the Ginzburg-Landau parameter κ, and the microscopic coherence length ξ as well as λ.

In order to directly determine the irreversibility line and compare it with the results obtained from the imaginary component of the AC susceptibility χ'', measurements of the zero field cooled and field cooled DC magnetization should be performed. Furthermore, to find the temperature dependence of the lower critical fields $H_{c1}(T)$ as well as the irreversible magnetization curve, it may be desirable to perform DC magnetization measurements in the mode where the applied field varies while the temperature is fixed. But this may turn out to be difficult for the same reasons as encountered in the previous measurements:[81] a). the possibility of introducing additional noise into the SQUID sensor; and b). the non-linear response of the background to the applied magnetic filed possibly due to unbalanced pick-up coils.

References:

1. J. G. Bednorz and K. A. Muller, *Z. Phys.* **B64**, 189 (1986).
2. M. K. Wu *et. al, Phys. Rev. Lett.* **58**, 908 (1987).
3. H. Maeda, Y.Tanaka, M. Fukutomi and T. Asano, *Jpn. J. Appl. Phys.* **27**, L209 (1988).
4. Z. Z. Sheng and A. M. Hermann, *Nature* **332**, 138 (1988).
5. Y. Tokura, H. Takagi and S. Uchida, *Nature* **337**, 345 (1989).
6. V. J. Emery, *Nature* **337**, 306 (1989).
7. P. W. Anderson, *Science* **235**, 1196 (1987). P. W. Anderson, *Phys. Rev. Lett.* **59**, 2497 (1987).
8. A. A. Abrikosov, *Soviet Phys. JETP* **5**, 1174 (1957).
9. V. L. Ginzburg, *Zh. Eksperim. i Teor. Fiz.* **23**, 236 (1952).
10. L. P. Gor'kov and T. K. Melik-Barkhudarov, *Soviet Phys.–JETP* **18**, 1031 (1964).
11. D. R. Tilley, *Proc. Phys. Soc.* (London) **86**, 289 (1965).
12. P. de Trey and Gygax, *J. Low Temp. Phys.* **11**, 421 (1973).
13. R. A. Klemm and J. R. Clem, *Phys. Rev.* **B21**, 1868 (1980).
14. V. G. Kogan, *Phys. Rev.* **B24**, 1572 (1981).
15. D. L. Kaiser et al., *Journal of Crystal Growth* **85**, 593 (1987).
16. W. Xing and O. Rajora, Unpublished.
17. A. W. Sleight, *Supercurrents* **8**, June 1988; A. W. Sleight, *Supercurrents* **9**, July 1989.
18. Y. Gao et al., *Science* **241**, 954 (1988).
19. J. M. Tarascon et al., *Phys. Rev.* **B 37**, 9382 (1988).
20. T. Kajitani et al., *Jpn. J. Appl. Phys.* **27**, L587 (1988).
21. T. M. Shaw et al., *Phys. Rev.* **B 37**, 9856 (1988).
22. D. Shindo et al., *Jpn. J. Appl. Phys.* **27**, L1018 (1988).
23. D. Song, W. Xing, S. Gygax, O. Rajora, and L. K. Peterson, Second Canadian

Symposium on High Temperature Superconductivity; Vancouver, October, 1988.

24. L. V. Azaroff, *Elements of X-Ray Crystallography,* Chapter 18.
25. *Handbook of Chemistry and Physics,* P. E-87, Edited by R. C. Weast, Published by CRC Press.
26. R. P. Giffard, R. A. Webb, and J. C. Wheatly, *J. Low Temp. Phys.* **6**, 533 (1972).
27. System 330 Operation Manual, SHE Inc., San Diego, USA.
28. Operational Manual, CTF Ltd., Burnaby, B. C. Canada.
29. M. Denhoff, S. Gygax, and J. R. Long, *Cryogenics* **41**, 400 (1981).
30. R. S. Tebble and D. J. Craik, *Magnetic Materials*, Section 1.1.
31. J. A. Osborn, *Phys. Rev.* **67**, 351 (1945).
32. D. J. Craik, *Structure and Properties of Magnetic Materials*, Section 1.6.1.
33. R. A. Klemm, *J. Low Temp. Phys.* **39**, 589 (1980).
34. R. Meservey and B. B. Schwartz, Superconductivity, Vol.1 P. 174, Edited by R. D. Parks.
35. A. Umezawa, et al., *Phys. Rev.* **B38**, 2843 (1988).
36. J. T. Lin et al., *Phys. Rev.* **B38**, 5095 (1988).
37. G. Shaw et al., *Physica* **C 162-164**, 341 (1989).
38. L. Krusin-Elbaum, A. P. Malozemoff, and G. V. Chandrasekhar,*Physica* **C 162-164**, 1553 (1989).
39. B. Batlogg et al., *Physica* **C 153-155**, 1062 (1988).
40. A. K. Grover et. al., *Pramana-J. Phys.* **30**, 569 (1988).
41. D. Shoenberg, *Superconductivity,* Appendix II.
42. Muhlschlegel, *Z. Phys.* **155**, 313 (1959).
43. J. Rammer, *Europhys. Lett.* **5**, 77 (1988).
44. S. Mitra, J. H. Cho, W. C. Lee, D. C. Johnston, and V. G. Kogan, *Phys. Rev.* **B40**, 2674 (1989).
45. V. G. Kogan, M. M. Fang, and S. Mitra, *Phys. Rev.* **B38**, 11958 (1988).
46. E. J. Ansaldo et. al.,*Physica* **C 162-164**, 259 (1989).

47. G. Aeppli et al., *Phys. Rev.* **B35**, 7129 (1988).

48. L. Krusin-Elbaum et al., *Phys. Rev. Lett.* **62**, 217 (1989).

49. A. T. Fiory et al., *Phys. Rev. Lett.* **61**, 1419 (1988).

50. D. R. Harshman et al., *Phys. Rev.* **B39**, 851 (1989).

51. K. A. Muller, M. Takashige, J. G. Bednorz, *Phys. Rev. Lett.* **58**, 408 (1987).

52. D. R. Nelson, et al., *Phys. Rev. Lett.* **60**, 1973 (1988).

53. P. L. Gammel, et al., *Phys. Rev. Lett.* **61**, 1666 (1988).

54. A. P. Malozemoff et al., *Phys. Rev.* **B38**, 7203 (1988).

55. Y. Yeshurun et al., *Phys. Rev. Lett.* **61**, 1658 (1988); Y. Yeshurun et al., Cryogenics 29, 258 (1989).

56. T. T. M. Palstra et al., *Phys. Rev. Lett.* **61**, 1662 (1988).

57. C. P. Bean, *Phys. Rev. Lett.* **8**, 250 (1962); C. P. Bean, *Rev. Mod. Phys.* **36**, 31 (1964).

58. Y. B. Kim et al., *Phys. Rev. Lett.* **9**, 306 (1962).

59. H. London, *Phys. Lett.* **6**, 162 (1963).

60. P. W. Anderson, *Phys. Rev. Lett.* **9**, 309 (1962).

61. T. Palstra et. at., Preprint, 1989.

62. Y. Yeshurum et. at., *Phys. Rev.* **B38**, 11828 (1988).

63. J. R. Clem, *Physica* **C153-155**, 50 (1988).

64. K.-H. Muller, Physica **C 159**, 717 (1989).

65. S. Gygax, *J. Low Temp. Phys.* **36**, 109 (1979).

66. D. E. Farrel, S. Bonham, J. Foster, Y. C. Chang, P. Z. Jiang, K. G. Vandervoort, D. J. Lam, and V. G. Kogan, Preprint (1989).

67. L. J. Campbell, M. M. Doria, and V. G. Kogan, *Phys. Rev.* **B38**, 2439 (1988).

68. V. G. Kogan, *Phys. Rev.* **B38**, 7049 (1988).

69. G. J. Dolan, F. Holtzberg, C. Feild, and T. R. Dinger, *Phys. Rev. Lett.* **62**, 2184 (1989).

70. B. Batlogg et al., *Physica* **C153-155**, 1062 (1988).

71. Y. Hidaka et al., *Jpn. J. Appl. Phys.* **27**, L538 (1988).

72. T. T. M. Palstra et al., *Phys. Rev.* **B38**, 5102 (1988).

73. M. J. Naughton et al., *Phys. Rev.* **B38**, 9280 (1988).

74. J. Y. Juang et al., *Phys. Rev.* **B38**, 7045 (1988).

75. R. B. van Dover et al., *Phys. Rev.* **B39**, 4800 (1989).

76. U. Welp et al., *Phys. Rev. Lett.* **62**, 1908 (1989).

77. J. R. Cooper et. al., *Nature* **343**, 444 (1990).

78. D. Larbalestier, Nature 343, 210 (1990).

79. T. R. Dinger et al., *Phys. Rev. Lett.* **58**, 2687 (1988).

80. G. W. Crabtree et al., *Phys. Rev.* **B36**, 4021 (1987).

81. M. W. Denhoff and S. Gygax, *Phys. Rev.* **B25**, 4479 (1982).